frontiers | Frontiers in Earth Science

TYPE Original Research
PUBLISHED 21 February 2025
DOI 10.3389/feart.2025.1512652

OPEN ACCESS

EDITED BY
Hao Shi,
Anhui University of Science and Technology, China

REVIEWED BY
Mahmoud Ebrahimi,
University of Maragheh, Iran
Vahab Sarfarazi,
Hamedan University of Technology, Iran
Riya Mondal,
Presidency University, India

*CORRESPONDENCE
Yunliang Yu,
yuyunliang@jlu.edu.cn

RECEIVED 17 October 2024
ACCEPTED 27 January 2025
PUBLISHED 21 February 2025

CITATION
Liu Y, Yu Y, Gao X, Cai H and He J (2025) Deep structure and Pb-Zn mineralization control of the Shuangdinggou-Xinling rock body in the Qingchengzi ore field revealed by gravity profile inversion.
Front. Earth Sci. 13:1512652.
doi: 10.3389/feart.2025.1512652

Deep structure and Pb-Zn mineralization control of the Shuangdinggou-Xinling rock body in the Qingchengzi ore field revealed by gravity profile inversion

Yingchun Liu, Yunliang Yu*, Xiangwei Gao, Hongchen Cai and Jinxin He

College of Earth Sciences, Jilin University, Changchun, China

The Qingchengzi region in Liaoning Province represents a significant Pb-Zn ore site in China. The Late Triassic Shuangdinggou-Xinling granite intrusions, located in both the southern and northern parts of this mineral-rich area, critically influence the genesis of Pb-Zn deposits. The limited investigation into the deep distribution characteristics of these granite bodies hinders our understanding of their potential for deep-seated mineral deposits. We conducted an integrated approach that encompassed geological surveys, geochemical analyses, and Bouguer gravity anomaly assessments. The geochemical investigations of the Shuangdinggou and Xinling granite bodies indicated analogous signatures, reinforcing their collective contribution to the generation of ore-forming fluids. Furthermore, the gravity data demonstrated that the Shuangdinggou and Xinling granite bodies are interconnected at depth, with the Shuangdinggou body exhibiting a burial depth ranging from approximately 4,000–4,500 m. By employing human-machine interactive gravity profile inversion across two cross-sections, we have clarified the extensive subsurface morphology of the granite formations and validated their hidden interconnections. In the Qingchengzi mining zone, the Xinling body (granite branch) extends northeastward from the Shuangdinggou body (granite base) along a fault. These granite intrusions jointly govern the formation and spatial distribution of Pb-Zn deposits, influenced by overlaps of syngenetic fractures resulting from magmatic intrusions and earlier tectonic folding events.

KEYWORDS

geochemistry, granite, Late Triassic, lithologic homology, lithologic deep structure, human-computer interactive (HCI) gravity profile inversion

1 Introduction

As a significant mineral resource center on the Liaodong Peninsula, the Qingchengzi ore field is well-known for its extensive polymetallic resources, primarily Pb-Zn deposits (Xie et al., 2021b). To date, 12 Pb-Zn deposits of varying scales have been identified in this area. Based on their genesis, these deposits are classified into

three types: layered deposits represented by Zhenzigou (Duan et al., 2014; Wei et al., 2021; Yanshen et al., 2021), vein deposits showcased by Xiquegou, and feather deposits illustrated by Benshan and Mapao (Duan et al., 2017). A comprehensive analysis of the diagenetic and ore-forming eras, as well as the sources of mineralization, indicate that these deposits are predominantly associated with the Indosinian magmatic process (Hao et al., 2023a; Wang et al., 2017b; Wei et al., 2022). Presently, the Pb-Zn deposits in Qingchengzi are arranged in a northeast-oriented strip along fault lines, primarily within the Gaojiayu Formation and the Dashiqiao Formation of the Liaohe Group (Zhang et al., 2022a). The development of mineralization within the Pb-Zn deposits revealed complex and multi-stage genesis characteristics, including the Paleoproterozoic synsedimentary mineralization, the Paleozoic Lvliang orogenic metamorphic-deformation hydrothermal mineralization, and the Mesozoic tectonic-magmatic-hydrothermal superposition mineralization. The three mineralization periods demonstrate rich and multi-stage mineralization processes (Li et al., 2019b; Zhou et al., 2020), contributing to the current distribution pattern of ore deposits. This pattern manifests as sedimentary-metamorphic-hydrothermal superimposed transformed deposits (Li et al., 2019a). Comprehensive research has revealed that the genesis of deposits across different mineral species in the ore concentration area is predominantly magmatic-hydrothermal, associated with Indosinian magmatic intrusion activities, with the Shuangdinggou rock body illustrating this magmatic activity (Hao et al., 2023b; Hao et al., 2023c; Liu et al., 2019a).

In the Qingchengzi ore concentration zone, the lead-zinc deposits predominantly stem from Mesozoic tectonic-magmatic activities, with their present attributes influenced by the third phase of mineralization occurring during the Late Triassic, which is marked by the superposition of tectonic magmatic and hydrothermal processes (Wu et al., 2022; Yang et al., 2012). Within the ore area, super positional modification of Late Triassic magmatic-hydrothermal fluids led to the onset of a granitic magmatic event within the Pb-Zn deposits (Tannous et al., 2018; Yang et al., 2021). This phenomenon resulted in the development of the Shuangdinggou granite body and Xinling granite body, with both bodies closely linked to Pb-Zn mineralization (Yu et al., 2009). The analysis of rare earth elements, sulfur, lead isotopes, and hydrogen and oxygen isotopes in the Shuangdinggou and Xinling rock bodies revealed an intricate relationship with Mesozoic Indosinian magmatism (Duan et al., 2024; Wei et al., 2023). The C-O-S-Pb isotopic and LA-ICP-MS analyses conducted on the surrounding rocks (carbonate rocks) of the Pb-Zn ore revealed a strong relationship between the ore-forming fluids of the Pb-Zn deposits and the Late Triassic magmatism (Li et al., 2020b; Li et al., 2020c; Sun et al., 2024a; Sun et al., 2024b). The sphalerite Zn/Cd values and pyrite Co/Ni values together suggest that the Pb-Zn ore-forming fluids are predominantly magmatic-hydrothermal (Li et al., 2020a; Sun et al., 2024a; Tan et al., 2021). The age characteristics of Rb-Sr and zircon U-Pb within the Pb-Zn deposits revealed the Rb-Sr age of sphalerite in the Zhenzigou Pb-Zn deposit to be 221 ± 12 Ma and pyrite in the Xiquegou Pb-Zn deposit to be 225 Ma (Sun et al., 2020b; Xu et al., 2020). Additionally, the zircon U-Pb age of the lamprophyre vein in the Nanshan Pb-Zn deposit was found to be 227 Ma (Duan et al., 2014; Fu et al., 2024; Sun et al., 2020a), and the zircon U-Pb age of granite porphyry veins in the Diannan Pb-Zn deposit was 232.8 ± 4.9 Ma (Di et al., 2020). The Pb-Zn deposits are of comparable age to the Late Triassic magmatic rocks, indicating that at least one stage of mineralization was strongly associated with the third stage of mineralization in the Mesozoic Late Triassic tectonic magmatic activation and re-emplacement (Wang et al., 2020). Geochemical characteristics, along with chronological studies, suggest that the deposits exhibit Late Triassic magmatic-hydrothermal mineralization, with a particular research focus on Indosinian Late Triassic magmatic activity (Jian et al., 2023; Jianbiao et al., 2024; Li et al., 2023a; Liu et al., 2019b; Pengfei et al., 2023). During deep drilling near the Late Triassic Shuangdinggou rock body, it was observed that Pb-Zn mineralization directly occurred within the granite porphyry. The Shuangdinggou rock body developed strong hydrothermal alteration such as silicification and pyrite mineralization, further suggesting that the Late Triassic intrusive rock body served as a source of ore-forming hydrothermal fluids (Duan et al., 2012). Magmatic-hydrothermal processes played a major role in the formation of the Qingchengzi Pb-Zn deposits. However, these deposits developed within Paleoproterozoic sedimentary layers found between the northern and southern Shuangdinggou and Xinling rock formations, without direct contact. Thus, it is hypothesized that there could be concealed interconnected areas deep inside the Late Triassic Shuangdinggou and Xinling rock bodies. These areas likely act as sources of hydrothermal fluids essential for the formation of Pb-Zn deposits in the layers above. Based on aeromagnetic data, there might be linkages between the Shuangdinggou and Xinling rock bodies at depth (Feng et al., 2010; Ibrahim et al., 2017). The Xinling rock body might be a branch of the Shuangdinggou rock body, which is part of a substantial granite batholith. Remote sensing and gravity magnetic data suggest a subsurface connection, indicating that they may represent a singular geological entity (Xie et al., 2018). Analyses of rare earth elements and isotopes further substantiate their genetic relationship (Wang et al., 2020), while zircon U-Pb dating reveals overlapping formation periods: 200–220 Ma for Shuangdinggou rock body and 225.3 ± 1.8 Ma for Xinling rock body (Duan et al., 2014; Li et al., 2020b). Analysis of the age and rare earth elements of the two rock formations reveals their contemporaneity and homologous nature. Although previous studies indicate potential connectivity between these formations at depth, the precise nature of this connectivity and the morphological distribution within their depths remains unclear. Consequently, we conducted a comprehensive analysis, employing a wide array of geological data encompassing fundamental geology, geochemistry, and geophysics, to examine the subsurface distribution patterns, interconnectivity, and geological development of the Shuangdinggou and Xinling rock bodies, along with their impact on Pb-Zn mineralization within the Qingchengzi mining region. This analysis incorporated human-machine interactive profile inversion to quantitatively assess the deep distribution characteristics of the interconnected regions between the two formations. The study clarified the scale, morphological distribution, occurrence states, and geometric topology of the deep segments of the intrusive rock body located in the Qingchengzi mining area. Moreover, we thoroughly examined the impact of tectonic activity on the formation of three distinct endowment states of Pb-Zn deposits, thereby establishing a scientific foundation for mineralization forecasting, deep exploration, and quantitative resource assessment, which

will aid in future geological exploration and mineral resource development.

2 Contribution

This research significantly advances our knowledge of the deep structural controls affecting Pb-Zn mineralization in the Qingchengzi ore field. It clarifies the geological interactions between the Shuangdinggou and Xinling granite formations. By applying gravity profile inversion, we reveal the intricate subsurface shapes and interconnections of these granite structures, underscoring their role in the development and positioning of Pb-Zn ore deposits. Our results suggest that mineralization is largely influenced by syngenetic fractures and folds associated with magmatic intrusions and prior geological processes. This study fills a vital gap in our understanding of the deep distribution characteristics of these rock formations. Additionally, it lays a foundational framework for future mineral exploration and resource assessment in comparable geological contexts, thereby improving predictive models for deep mineral resources.

3 Geological setting

The Qingchengzi Pb-Zn ore concentration area is situated within the eastern part of Dandong, Liaoning Province, China, on the northeast edge of the North China Plate (An et al., 2022). Located in the northwest of Fengcheng City, Dandong City, Liaoning Province, China, its administrative boundaries range between 123°30′–123°45′E and 40°40′–40°50′N (Figure 1A). The geotectonic region is located to the east of the Tantanlu Fault, within the axial region of the Liaoji Rift Belt (Li et al., 2020b), at the intersection of the Paleo-Asian Oceanic Tectonic Domain and the Pacific Rim Tectonic Domain (Yang and Wu, 2009). The Liaoji Rift Zone, situated between the Longgang Plot and the Wolfforest Plot in the Archean (Figure 1B) (Quan et al., 2023; Song et al., 2017), serves as an interland rift formed by crustal tensional rifting-rapid subsidence-return extrusion during the Paleoproterozoic period. It extends in a nearly east-west direction (Lin et al., 2011). The rift zone predominantly comprises three tectonic phase zones: the central depression zone, the northern margin slope zone, and the southern margin shallow platform zone. The ore concentration area is situated within the central depression zone (Figure 1B) (Yu et al., 2009). During the extensional fracturing stage, the lower crust melts and intrudes the Paleoproterozoic Liaoji granite due to crustal stretching and subsidence, thus forming gentle and open folds as well as leads to structural features such as the Jianshanzi Fault and the Yushanggou Fault (Yang and Li, 2023). The ore-forming hydrothermal fluid mixes with seawater along the contemporaneous fault at the edge of the basin and precipitates along with diagenetic materials, forming an initial ore source layer rich in Pb, Zn, and S. Layered ore bodies are formed in certain ore source layers (Ma et al., 2016; Wu et al., 2024). The subsidence of the Earth's crust led to the stratigraphic development of the Gaojiayu Formation (Pt_1 g) at the bottom of the Liaohe Group and the Dashiqiao Formation (Pt_1d) in the central part of the study area (Chen et al., 2024). Simultaneously, the co-sedimentary Liaoji granite continued to intrude, forming vein-like Pb-Zn ore bodies *in situ* or favorable structural areas characterized by magma upwelling (Ma et al., 2013). The upward intrusion of Indosinian granites along north-east trending faults caused enrichment of Paleoproterozoic layered ore bodies, thereby forming vein-like and plume-like Pb-Zn ore bodies. The retrograde compression led to the formation of a series of compound folds, secondary faults, and the Gaixian Formation strata at the top of the Liaohe Group (Pt_1gx) (Wang et al., 2017a).

In this region, the Paleoproterozoic striated granite serves as the foundation (Song et al., 2017), primarily leading to the development of the Paleoproterozoic Liaohe Group stratigraphy, including the Lieryu Formation, the Gaojiayu Formation, the Dashiyqiao Formation, and the Gaixian Formation in the ascending order of age (Di et al., 2020; Wu et al., 2022). The stratigraphy exposed at the Qingchengzi ore area predominantly comprises the Gaojiayu Formation, Dashiqiao Formation, and Gaixian Formation (An et al., 2022). The Gaojiayu Formation is relatively thin compared to other strata, with a thickness of 100–600 m. It is primarily distributed in the southern part of the mine area, and its lithology predominantly comprises amphibolite schist, granulite, interbedded schist, and marble (Yang and Li, 2023). The Dashiqiao Formation exhibits the most extensive distribution in this area and is characterized by a significant variation in rock thickness, generally ranging from 1,000 to 1,500 m, with a maximum thickness of up to 3,800 m. It serves as the major ore-endowed layer of the Pb-Zn deposits (Sun et al., 2020a). This layer can be divided into three segments: the first segment (Pt_1d_1) predominantly comprising marble, diorite, diopside, granulite, schist, and slate, with a thickness of 500 m; the second segment (Pt_1d_1) primarily comprising schist, gneiss, sandstone, granulite, diorite, and diopside, with a stratigraphic thickness of 100–500 m; and the third segment (Pt_1d_3), widely exposed in the central-southern part of the study area, characterized by lithologies primarily comprising marble, schist, amphibolite, and granulite, with a stratigraphic thickness of 500 m (Zhang et al., 2022b). The Gaixian Formation is widely exposed and serves as the major ore-bearing layer of the gold and silver deposits in this area. It is primarily composed of biotite schist, sillimanite mica schist, biotite granulite, etc., with a weathering and denudation residual thickness of about 300 m (Wang et al., 2017a; Yu et al., 2022).

Folds and faults relatively exhibit significant development in the ore concentration area. Particularly, the fold structures in the Paleoproterozoic Liaohe Group stratigraphy from north to south include the Xinling anticline, Sikeyangshu syncline, Zhenzigou anticline, and Nanshan syncline (Li et al., 2019b). Based on their orientations, the fault structures can be classified into three types: north-east, north-west, and near-north-south (Figure 1C) (Sun et al., 2022). The north-east trending Erdaogou Fault and the north-west trending Jianshanzi Fault serve as the two major faults within the Qingchengzi ore field. These faults constitute the major rhombic fracture tectonic framework in the area, controlling the large-scale spatial distribution of the ore bodies (Di et al., 2020; Xu et al., 2020). They serve as the primary ore-conducting and ore-holding structures for vein and feather-shaped ore bodies. The secondary faults in the near SN and EW directions within the diamond-shaped fault structure framework serve as the major ore-holding structures for layered Pb-Zn deposits within the mining area (Yu et al., 2021).

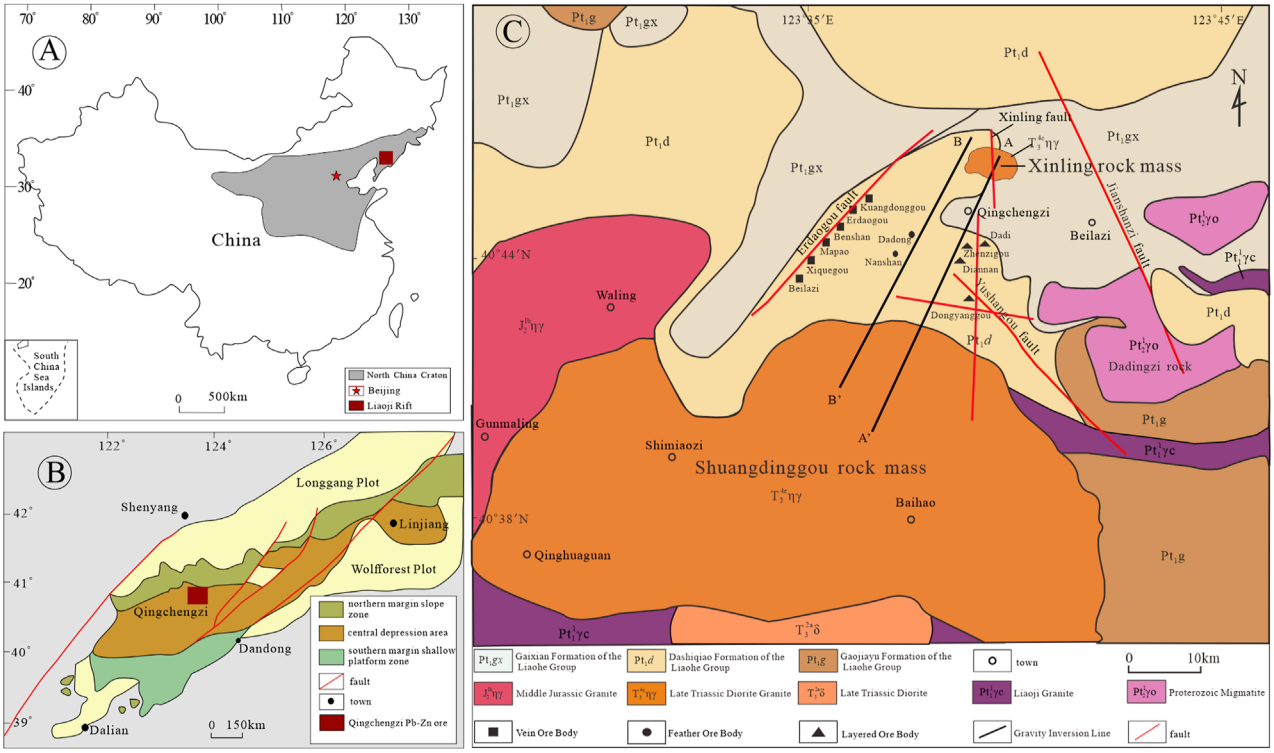

FIGURE 1
Regional Geologic Background modified after (Xie et al., 2018); **(A)** Location of Qingchengzi orefield **(B)** Sketch map of the Liaoji rift zone with the location of the Qingchengzi orefield; **(C)** Geological map of the Qingchengzi orefield after (Duan et al., 2017).

The northeast direction is represented by the Erdaogou Fault, which has a strike of 30°–60° and a dip of 70°–90° (Xiao et al., 2023). The vein-shaped Pb-Zn deposits in Beilazi, Xiquegou, Mapao, Benshan, Erdaogou, and Kuangdonggou are distributed from the northeast to the southwest along the Erdaogou Fault (Li et al., 2020c). The Jianshanzi Fault strikes NW, with a fault width of 10–20 m and a tilt of 60°–90° towards NE (Xiao et al., 2023). The northwest-oriented Yushanggou Fault, with a strike of about 330° and a dip angle ranging from 30° to 45° (Li et al., 2019a; Yu et al., 2021), is located near the fault, with layered Pb-Zn deposits in Zhenzigou, Dadi, Diannan, and Dongyanggou and feather-shaped Pb-Zn deposits in Dadong and Nanshan. The near-north-south-oriented Xinling Fault is developed along the axis of the Xinling anticline and is speculated to be a channel for upward intrusion of the Xinling rock body.

The magmatic activities in the Qingchengzi ore area was relatively high, especially during the Paleoproterozoic and Mesozoic periods (Duan et al., 2024; Li et al., 2023b). The granite exposed in the Qingchengzi ore field originated during the magmatic activity periods of the Paleoproterozoic, Middle Proterozoic, Late Triassic, and Yanshanian (Sun et al., 2020a). The Paleoproterozoic granite is represented by the Dadingzi monzonite (Wang et al., 2017a), which was involved in the folding of the Liaohe Group and experienced synchronous deformation along with the Liaohe Group strata. It is strongly associated with layered and quasi-layered Pb-Zn mineralization. During the Middle Proterozoic, magmatic intrusion activity was weak and primarily characterized by the development of the Dadingzi granite and the Fangjiaweizi granite (Xie et al., 2021a).

During the Mesozoic Indosinian period, the magmatic intrusion activities were very strong, resulting in the formation of intermediate and plutonic rock bodies. These rock bodies are represented by the Mesozoic Late Triassic Shuangdinggou granite body and the Xinling granite body (Chen et al., 2005), which are exposed on the north and south of the Qingchengzi mining field, respectively. The Yanshanian granite, situated adjacent to the northwest of the Shuangdinggou rock body, is prominent in the Gunmaling-Waling area. The Middle Paleoproterozoic granite and Yanshanian granite do not contribute to the mineralization of Pb-Zn deposits in the mining area (Figure 1C) (Ma et al., 2022). The streak-like granitic intrusive rock body developed in the Paleoproterozoic era is known as Liaoji granite (Zhang, 1987). This granite appears throughout the southern and western regions of the Shuangdinggou rock body within the study area, showing large and banded exposures. It extensively underlies the Liaohe Group strata, partially intruding into both the Gaojiayu Formation and the Dashiqiao Formation, with certain sections visible at the surface (Gao et al., 2023).

4 Analysis of petrophysical and geochemical elements

4.1 Petrophysical characteristics of Shuangdinggou-Xinling rock body

The Shuangdinggou rock body outcrop in the southern part of the Qingchengzi Pb-Zn ore area appears as a rock foundation

TABLE 1 Dating data for Shuangdinggou and Xinling intrusions.

Test area	Method	Age (Ma)	Source
Shuangdinggou	Zircon U-Pb	216.4 ~ 219.3 200 ~ 220 223 ~ 225.4 225.7 ~ 235.7 200 ~ 220	Zhou et al. (2017) Duan et al. (2012) Jiang and Wei (1989)
	K-Ar	236 ~ 246 231 224 ~ 227	Jiang and Liu (1990)
Xinling	Zircon U-Pb	223.5 ~ 227.1 225	Yu et al. (2009)
	K-Ar	214 ~ 231 218 ~ 227 217.6 ~ 226.7 214 ~ 229	Jiang and Liu (1990)

with an exposed area of 300 km^2 (Duan et al., 2014). The long axis of the rock body extends along the east-west direction, primarily influenced by the nearly east-west tectonic forces (Duan et al., 2014). Additionally, Pb-Zn polymetallic ore deposits are distributed within the outer contact zone of the rock body (Li et al., 2023a). The porphyritic monzonitic granite reveals a porphyritic texture and comprises porphyritic crystals and a matrix. The porphyritic crystals mainly consist of alkaline feldspar, typically measuring 1–3 mm, while the matrix includes alkali feldspar, plagioclase, and quartz (Ezzeddine and Sultan, 2022; Xie et al., 2018).

The Xinling rock body outcrop in the Xinlinggou area at the center of the Qingchengzi ore area is intrusively connected with the Dashiqiao Formation. It is formed as a rock stock with an exposed area of 2 km^2, influenced by east-west structures (Li et al., 2023a). The lithology is monzonitic granite, with plagioclase, alkali feldspar, and quartz as phenocrysts. The mineral assemblage mainly consists of alkali feldspars (approximately 45%), quartz (20%–25%), plagioclase (20%–25%), and biotite (around 2%). The matrix exhibits a microcrystalline texture, typically containing feldspar, quartz, and biotite microcrystals, along with some daisy crystals and glassy substances (He et al., 2023).

Between the 1990s and the early 21st century, researchers used the zircon U-Pb dating technique to determine that the Shuangdinggou rock body formed between 200 Ma and 235.7 Ma. In contrast, the Xinling rock body dated between 223.5 Ma and 227.1 Ma. The K-Ar dating method indicated that the Shuangdinggou rock body fell within 224 Ma to 246 Ma, while the Xinling rock body ranged from 217.6 Ma to 231 Ma. Consequently, both rock bodies are classified as Mesozoic Indosinian formations with nearly equivalent ages (Table 1).

4.2 Major elements

Table 2 presents the average compositional data obtained from 13 samples of the Shuangdinggou rock body and seven samples of the Xinling rock body. The results indicate that the average concentrations of the primary elements in the Shuangdinggou-Xinling rock body are equivalent. For the Shuangdinggou rock body, $\omega(SiO_2)$ ranges from 66.78% to 75.33%, averaging 70.32%. The magnesium oxide content, $\omega(MgO)$, varies between 0.3% and 1.61%, with an average of 1.0%. Iron content shows $\omega(FeO)$ from 0.6% to 2.55% and $\omega(Fe_2O_3)$ from 0.33% to 3.9%, averaging 1.34%. Sodium oxide levels, expressed as $\omega(Na_2O)$, range from 2.7% to 5.03%, averaging 3.96%. The potassium oxide content, $\omega(K_2O)$, measures between 3.53% and 5.22%, with an average value of 4.44%. Additionally, the ratio of sodium to potassium, $\omega(Na_2O)/\omega(K_2O)$, falls between 0.76 and 0.96. Notably, the rock body exhibits significant aluminum presence, with $\omega(Al_2O_3)$ ranging from 12.46% to 14.48%.

In the Xinling rock body samples, silica (SiO_2) concentrations range from 63.16% to 78.58%, averaging 69.11%. Magnesium oxide (MgO) content varies from 0.32% to 2.02%, with a mean of 1.07%. Iron oxide components include ferrous iron (FeO) from 1.47% to 2.8% and ferric iron (Fe_2O_3) from 0.49% to 3.16%, averaging 1.45%. The samples indicate a rich iron composition. Sodium oxide (Na_2O) shows levels between 2.27% and 5.04%, averaging 3.95%, while potassium oxide (K_2O) ranges from 4.32% to 6.81%, with an average of 5.20%. The sodium to potassium ratio (Na_2O/K_2O) is between 0.525 and 0.74, indicating a relative abundance of potassium. Similar to the Shuangdinggou rock body, this sample also exhibits substantial aluminum oxide (Al_2O_3) content, ranging from 8.97% to 14.31%.

The TAS illustration (Figure 2) indicates that 13 samples originate from the Shuangdinggou rock body. Among these, 10 sampling points lie within the granite zone, making up 76.9% of the total points. The remaining three points fall within the quartz monzonite and granodiorite areas, constituting 23.1%. For the Xinling rock body, seven samples were collected. Here, four samples come from the granite zone, comprising 57.1% of the total, while three samples originate from the quartz monzonite and granodiorite regions, amounting to 42.9%. In the SiO_2-K_2O diagram (Figure 3), seven injection points from the Shuangdinggou rock body are found in the potassium basalt area, representing 53.8% of the samples. Additionally, six injection points appear in the high-potassium-calcium alkaline series region, which accounts for 46.2%. In the Xinling rock body samples, six

TABLE 2 Average major element contents (%) in Shuangdinggou and Xinling intrusions.

Intrusion	Shuangdinggou	Xinling
SiO_2	70.32	69.11
TiO_2	0.43	0.36
Al_2O_3	13.41	13.35
Fe_2O_3	1.34	1.45
FeO	1.75	1.74
MnO	0.04	0.03
MgO	1.00	1.07
CaO	0.90	1.25
Na_2O	3.96	3.95
K_2O	4.44	5.20
P_2O_5	0.18	0.11
A/CNK	1.30	1.28
A/NK	1.60	1.46
δ	2.58	3.21

[a]Note: The data for the Shuangdinggou Intrusion and Xinling Intrusion are cited from the literature (Dong et al., 2010; Duan et al., 2012; Jiang and Wei, 1989).

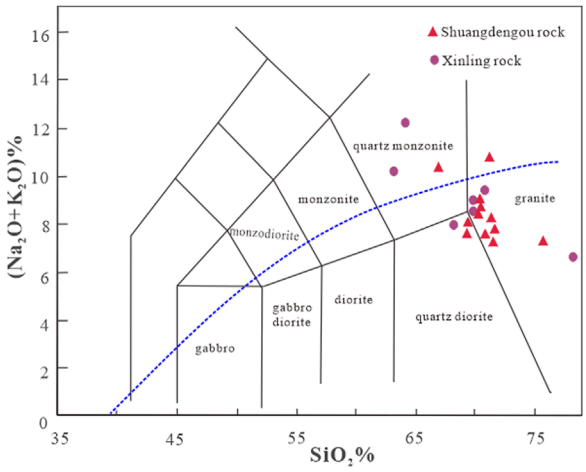

FIGURE 2
TAS diagrams of the Shuangdinggou-Xinling rock body after (Duan et al., 2014). Number of samples located in the granite, quartz diorite and granodiorite areas of the two rock bodies.

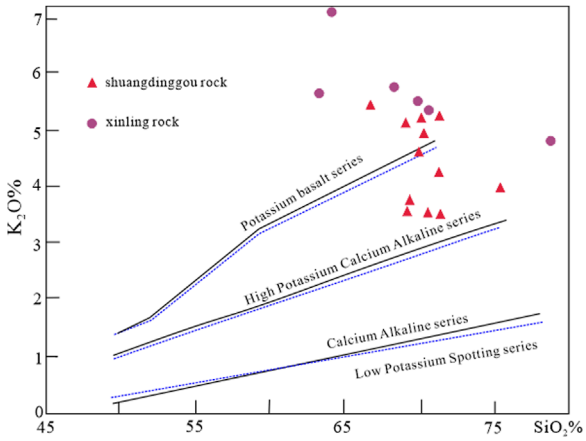

FIGURE 3
SiO_2 versus K_2O relationship for the Shuangdinggou-Xinling rock body. Number of samples from two bodies located in the potassium basalt region and in the high potassium-calcium-alkaline series region.

derive from the potassium basalt area, 85.7% of the total. Only one sample is from the high potassium-calcium alkaline series, equating to 14.3%. The A/NK-A/CNK plot (Figure 4) displays that one sampling point of the Shuangdinggou rock body lies in the quasi-aluminous region, while the remaining 12 are within the peraluminous region. Conversely, all samples from the Xinling rock body are sourced from the peraluminous area. When these sampling results align with the TAS statistical outcomes, it is evident that both rock bodies showcase high silicon and aluminum levels concurrently. Figure 4 demonstrates elevated A/NK values for both rock bodies exceeding 1, with their A/CNK values surpassing 1.1. The elemental traits outlined indicate that both rock bodies possess S-type granite characteristics, primarily attributed to the melting of crustal materials alongside potential assimilation of mantle-sourced materials.

4.3 Rare earth elements

The analytical findings of rare earth elements within the Xinling and Shuangdinggou rock formations (Table 3) reveal significant variation in the total concentration of rare earth elements in the Shuangdinggou formation, with ΣREE ranging from (188.04–482.609) × 10^{-6} (mean = 304.75 × 10^{-6}). In contrast, the Xinling formation exhibits a ΣREE of 82.12–142.86 × 10^{-6} (mean = 123.68 × 10^{-6}).

LREE/HREE denotes the ratio of light rare earth elements to heavy rare earth elements. In the Shuangdinggou rock body, the ΣLREE averages between (173.37–456.31) × 10^{-6}, with an average of 284.32 × 10^{-6}, while the ΣHREE ranges from (4.67–24.047) × 10^{-6}, yielding an average LREE/HREE of 13.82. Conversely, the Xinling rock body shows ΣLREE values from (64.19–129.48) × 10^{-6}, averaging at 109.47 × 10^{-6}, with ΣHREE spanning (12.42–17.93) × 10^{-6}, resulting in an average LREE/HREE of 8.11. The data indicates that the mean LREE/HREE ratio for both geological formations surpasses 8, demonstrating a significant enrichment of light rare earth elements. For the Xinling rock body, $(La/Yb)_N$ ranges from 13.24 to 50.44, whereas the Shuangdinggou rock body records $(La/Yb)_N$ values between 47.11 and 110.16. This indicates significant differentiation between light and heavy rare earth elements, combined with substantial enrichment of light rare earth elements and a relative scarcity of heavy rare earth elements in both bodies.

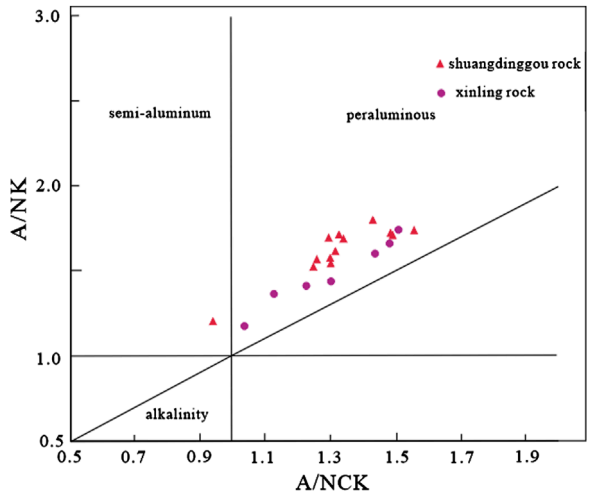

FIGURE 4
A/NK-A/NCK illustration of the Shuangdinggou and Xinling rock body. Number of samples from two bodies located in the quasi-aluminous basalt region and in the peraluminous region.

Figure 5 reveals that the distribution curves of rare earth elements in both Shuangdinggou and Xinling rock bodies demonstrate similar patterns. Each rock body displays varying degrees of positive cerium (Ce) anomalies and negative europium (Eu) anomalies. Table 3 indicates that the average δCe variation for Shuangdinggou is 2.94, while the average δEu is 0.27. For Xinling, the average δCe is 2.86 and δEu is 0.21. Both rock bodies show an enrichment of light rare earth elements and a depletion of heavy rare earth elements, with negligible significant fractionation. Furthermore, they exhibit characteristics of positive Ce anomalies, negative Eu anomalies, and considerable fractionation of heavy rare earth elements. These features suggest that both rock bodies derive from crustal sources, and their geochemical element compositions reflect a shared origin.

4.4 Isotopic characteristics

4.4.1 Pb isotope

The lead (Pb) isotopic composition of the Shuangdinggou rock formation closely resembles that of the Xinling rock formation. The measurements reveal $^{206}Pb/^{204}Pb$ ratios ranging from 16.417 to 17.41, $^{207}Pb/^{204}Pb$ from 15.459 to 15.525, and $^{208}Pb/^{204}Pb$ from 35.434 to 37.885 for Shuangdinggou. In contrast, the Xinling rock formation displays a broader range in its Pb isotopic composition, with $^{206}Pb/^{204}Pb$ ratios between 17.028 and 17.087, $^{207}Pb/^{204}Pb$ from 15.5 to 15.535, and $^{208}Pb/^{204}Pb$ from 37.322 to 37.885 (Table 4). This significant variability in isotopic data indicates that the lead in both formations primarily derives from the Earth's crust and suggests that these granite formations exhibit characteristics consistent with remelting processes.

4.4.2 S isotope

The Shuangdinggou rock body exhibits a sulfur isotopic composition of ^{34}S = 7.0‰–7.6‰, averaging 7.4‰. In contrast, the Xinling rock body shows a composition of ^{34}S = 5.6‰–6.3‰, with an average of 6.7‰ (Table 5). Both average values align within the isotopic range typical for S-type granite (−9.4‰–7.6‰), thereby affirming that these rock bodies are classified as S-type granite. Furthermore, the sulfur isotopic properties of these two rock bodies markedly differ from those found in meteorite sources. This disparity suggests a significant influx of crustal materials and indicates a lack of sulfur homogenization throughout their formation process.

4.4.3 H-O isotope

The hydrogen-oxygen isotope analysis of quartz from the Qingchengzi ore field shows notable variations in $\delta^{18}O_{SMOW}$ values across different geological formations, ranging from 2.8‰ to 6.0‰. The δD_{SMOW} values for quartz inclusion water fall between −78‰ and −100‰. In addition, the δDSMOW values for quartz in adjacent rocks range from 6.6‰ to 9.4%, while those for quartz inclusion waterfall within −81‰ to −91‰. In the Shuangdinggou and Xinling formations, closely associated with mineralization, the $\delta^{18}O_{SMOW}$ values of quartz or biotite water vary from 9.1‰ to 9.3‰, with δD_{SMOW} values between −81‰ and −85‰. Analysis of hydrogen and oxygen isotopes from surrounding rocks and ores indicates similar patterns, suggesting a consistent hydrothermal source. Furthermore, the hydrothermal fluids in the Qingchengzi ore field primarily consist of a mix of natural waters from various origins. Magmatic water and atmospheric precipitation dominate these origins during the initial mineralization phase. During the later stages, the share of atmospheric precipitation increased. However, the proportion of atmospheric precipitation increased during the late stage of mineralization (Wang et al., 2016; Zhang et al., 2019b).

Through the analysis of geochemical elements in the Shuangdinggou-Xinling rock body, we have a certain understanding of the mineral in the two rock bodies (Al-Ghoul and Sultan, 2019; Ibrahim and Sultan, 2023). This understanding established a strong geological basis for our inversion model. It facilitated the precise calibration of physical parameters for the rock formations. During the inversion, we designated a density of 2.59 g/cm^3 for both the Shuangdinggou and Xinling rock bodies. We also refined other model parameters based on their main elemental compositions. These adjustments markedly improved the accuracy and reliability of our inversion findings.

5 Methods and results

5.1 Rock physical parameters

The study area shows an average density of 2.7 g/cm^3 for the Paleoproterozoic Liaohe Group strata. However, the density varies across different layers. The Gaixian Formation possesses the highest density, averaging 2.78 g/cm^3. Next is the Dashiqiao Formation, which occupies the largest exposed area, with a density of 2.72 g/cm^3. The Gaojiayu Formation follows closely, averaging 2.7 g/cm^3. In contrast, the Paleoproterozoic Liaoji granite has a common density of 2.54 g/cm^3, while the Late Triassic acidic intrusive rocks from the Indosinian period measure 2.61 g/cm^3, representing the Shuangdinggou-Xinling granite body. The Late Triassic neutral intrusive rocks exhibit a relatively elevated

10.3389/feart.2025.1512652

TABLE 3 Rare earth element contents and characteristic values of the Xinling and Shuangdinggou rock bodies (10^{-6}).

Rare earth elements	Xinling rock body				Shuangdinggou rock body							
La	36	35.31	16.29	35.30	141.0	77.50	79.30	57.30	72.40	86.90	79.30	49.47
Ce	48	62.11	30.77	62.10	213.0	118.0	119.0	119.0	145.0	150.0	147.0	83.68
Pr	8.3	4.14	3.23	6.50	22.70	12.70	13.50	12.30	14.20	15.60	13.20	8.48
Nd	22	20.70	10.71	20.70	69.90	40.50	45.40	43.10	47.30	50.80	42.90	25.88
Sm	3.4	2.95	2.76	4.19	8.13	5.04	5.71	5.89	6.33	6.40	5.35	4.65
Eu	0.9	0.40	0.43	0.69	1.58	1.13	1.37	1.31	1.53	1.19	1.43	1.21
Gd	2.3	2.95	1.99	2.95	5.63	3.56	3.73	4.17	4.47	4.50	3.82	3.04
Tb	0.3	0.40	0.66	0.40	0.67	0.44	0.47	0.55	0.61	0.58	0.44	0.47
Dy	1.0	1.65	6.27	2.65	3.11	1.98	2.15	2.48	2.74	2.64	2.07	2.44
Ho	0.4	0.25	0.85	0.25	0.50	0.33	0.35	0.42	0.46	0.42	0.34	0.44
Er	0.9	0.38	0.77	0.34	1.41	0.93	0.94	1.21	1.24	1.23	0.95	0.94
Tm	0.10	0.08	0.15	0.08	0.21	0.14	0.14	0.18	0.20	0.18	0.14	0.15
Yb	0.90	0.70	1.23	0.70	1.28	0.87	0.87	1.16	1.11	1.12	0.90	1.05
Lu	0.10	0.11	0.19	0.11	0.19	0.15	0.14	0.19	0.18	0.18	0.13	0.16
Y	7.10	5.90	5.82	5.90	13.30	9.23	9.55	11.70	12.10	12.20	9.54	5.98
ΣREE	131.7	138.03	82.12	142.86	482.61	272.49	282.62	260.95	309.86	333.94	307.52	188.04
Lree	118.6	125.61	64.19	129.48	456.31	254.87	264.28	238.90	286.76	310.89	289.18	173.37
HREE	13.1	12.42	17.93	13.38	26.30	17.62	18.34	22.05	23.10	23.05	18.34	14.67
Lree/HREE	9.05	10.11	3.58	9.68	17.35	14.46	14.41	10.84	12.41	13.49	15.77	11.82
$(La/Yb)_N$	40.00	50.44	13.24	50.43	110.16	89.39	90.94	49.40	65.23	77.59	88.11	47.11
δCe	2.17	3.15	3.15	2.97	2.60	2.62	2.56	3.42	3.35	2.93	3.18	2.89
δEu	0.32	0.14	0.18	0.19	0.23	0.26	0.29	0.26	0.28	0.22	0.31	0.31
La/Sm	10.59	11.97	5.90	8.42	17.34	15.38	13.89	9.73	11.44	13.58	14.82	10.64
Gd/Yb	2.56	4.21	1.62	4.21	4.40	4.11	4.28	3.59	4.03	4.02	4.24	2.90

[a]Note: The data for this experiment were derived from (Dong et al., 2010; Duan et al., 2012).

density, particularly the medium and fine-grained granodiorite south of Qinghe-Tanggou, averaging 2.74 g/cm^3. This suggests significant differences in density traits among intrusive rocks with varying chemical compositions. Furthermore, the common density of acidic intrusive rocks from the Middle Jurassic of the Yanshanian is 2.59 g/cm^3, linked to the Gunmaling-Waling monzonitic granite (Chen et al., 2024). This reinforces the relationship between intrusion period and rock density. Density variations among geological units in the study area are substantial, with the Paleoproterozoic strata displaying the highest density. Notably, significant density differences appear within the area's acidic intrusions. Generally, earlier intrusion periods indicate higher rock body density, with neutral intrusive rocks demonstrating greater density than acidic intrusions.

5.2 Characterization of the Bouguer gravity anomaly and analytical extensions

The Bouguer gravity anomaly data obtained from the 2012 China Geological Survey database indicates notable positive anomalies within the northern Shuangdinggou rock body (HG_1) and the northeastern Xinling rock body (HG_1), with values fluctuating between 0.2 and 9.3 mGal. The Xinling rock body,

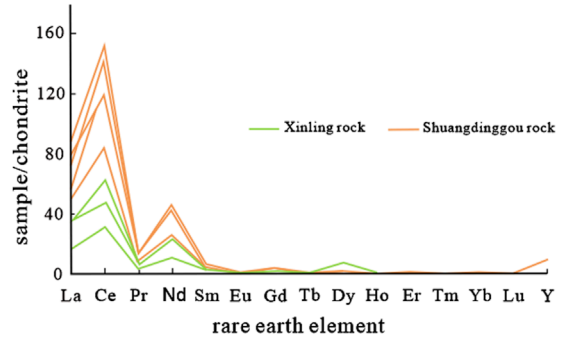

FIGURE 5
Comparison of rare earth element partition curves between Shuangdinggou and Xinling rock body.

characterized by its shallow depth and reduced density, is masked by the elevated gravity values of the adjacent Liaohe Group formations. The positive anomalies detected in the southern Shuangdinggou (HG_4) are attributed to the presence of denser Late Triassic granodiorite. Figure 6 illustrates an isopleth map that delineates these Bouguer gravity anomalies across the study area. The median gravity anomaly values (MG_1) imply that the Shuangdinggou rock body exhibits a lower density compared to the Liaohe Group strata. Negative gravity anomalies (LG_1, LG_2) identified at Qinghuaguan and Baihao suggest the existence of deeper magma intrusion centers. The density of granitic rocks within the upward intrusion channels is relatively low, resulting in localized negative anomalies. A minor positive anomaly is recorded in Shimiaozi (HG_5), where the Shuangdinggou rock body is at its thinnest and aligns with the Liaohe Group. Further analysis of gravity anomalies (MG_2, MG_3) reveals median zones resulting from the superposition of high-density Liaohe Group strata and low-density Liaoji granite. Localized negative anomalies in the Gunmaling-Waling and Daomaoshan regions (−15.1 to −5.5 mGal) are associated with low-density granites from the Middle and Early Jurassic periods, reflecting the density variations present within the geological formations of the study area.

The peak density of the Liaohe Group strata aligns with the pronounced local positive gravity anomaly. The acidic intrusive rocks from the Late Triassic and Middle-Late Jurassic have lower elevations than their neighboring rocks, correlating with regions exhibiting local negative gravity anomalies. In contrast, the medium-basic intrusive rocks from the Late Triassic show higher density relative to adjacent formations, contributing to local positive gravity anomalies. The extensive presence of Liaoji granite in the research area results in varied stacking configurations of the dense Liaohe Group strata with the less dense Liaoji granite and the low-density Shuangdinggou rock unit. This interlayering generates a median gravity anomaly zone through the combination of high and low densities. Moreover, the distribution of Bouguer gravity anomalies in this area clearly reflects significant density variations among strata and intrusive rocks from different geological periods and lithologies. These observations provide a solid framework for utilizing gravity anomaly fields to clarify the subsurface morphology of rock bodies.

5.3 Analysis of upward extension

The gravity anomalies in the study area extend upward by 500 m, 1 km, 2 km, 5 km, 8 km, and 10 km (Figure 7). As this upward extension increases, the gravity anomalies reveal a clear east-west striped-banded distribution. Positive anomalies arise from the high-density Liaohe Group in the north (LG_1), while negative anomalies are due to the low-density Late Jurassic medium-fine-grained monzogranite in the south (LG_4). These elements gradually erode the central median gravity anomaly zone (MG_1). The gravity anomaly map, extending up to 10 km, shows that MG_1, housing the lower density Shuangdinggou rock body, converges with the minimum gravity negative anomaly area (LG_3) caused by the low-density Middle Jurassic granite found at Gunmaling-Waling and the Houjiapuzi median gravity anomaly area (MG_3). This convergence forms an east-west-oriented striped-banded median gravity anomaly area, correlating with the extensive distribution of low-density Liaoji granite in the region. Thus, it indicates that the gravity anomalies related to the Shuangdinggou and Gunmaling-Waling rock bodies completely vanish when extended to 10 km. The burial depth of the geological body reflected at the extension site is about half of the extension height (Liu et al., 2019a), suggesting that the bottom burial depth of the Shuangdinggou rock body is less than 5 km. The local gravity anomaly (HG_4) caused by the denser Late Triassic medium-fine-grained granodiorite, south of Qinghe-Tanggou, vanishes completely when extended to 8 km. This suggests that the base of this rock formation lies buried at a depth of less than 4 km. The low-value gravity-negative anomaly (LG_1) in the western section of the Shuangdinggou rock body decreases progressively as the upward extension increases from 0 m to 2 km. At 5 km of extension, while the Qinghuaguan area still shows gravity-negative anomalies, it is now on the edges of the negative anomalies associated with Gunmaling-Waling (LG_3). Consequently, when these anomalies are extended upward by 5 km, the gravity-negative anomalies in the western and eastern regions of the Shuangdinggou rock (LG_1, LG_2) completely disappear. This confirms that the base of this rock body is at a shallow depth exceeding 4 km. Furthermore, this disappearance signals the loss of the gravity anomaly associated with the main retained sections of the magma intrusion channels deep within the Shuangdinggou rock body. As the upward extension increases, the northern section of the gravity anomaly median zone (MG_1) linked to the Shuangdinggou rock body starts to be progressively overshadowed by the positive gravity anomaly in the northern area of the study. In contrast, the southern part of the gravity anomaly median zone (MG_1) is increasingly obscured by the negative gravity anomaly in the southern area of the study upon reaching an 8 km extension. This indicates that the burial depth of the southern base of the rock body is deeper than that of the northern base, creating a configuration that is thinner in the north and thicker in the south.

5.4 Obtain residual gravity anomalies

This study analyzes and compares data to extract residual gravity anomalies using three distinct methods: the upward extension method, the vertical first-order derivative method, and the radial average power spectrum method. The results show that the average

TABLE 4 Lead Isotope Composition of Shuangdinggou and Xinling rock bodies.

Sample number	Test mineral	Rock	$^{206}Pb/^{204}Pb$	$^{207}Pb/^{204}Pb$	$^{208}Pb/^{204}Pb$	Source
SDB-2	Feldspar	Shuangdinggou	16.417	15.477	35.434	Chi (2002)
04LN676	Plagioclase		17.41	15.525	37.874	Li et al. (2020a)
04LN677	Plagioclase		17.121	15.483	37.863	
04LN678	Plagioclase		17.201	15.471	37.841	
04LN679	Plagioclase		17.159	15.459	37.885	
04LN681	Plagioclase	Xinling	17.028	15.535	37.51	
XDB-2	Feldspar		17.087	15.5	37.322	Chi (2002)
XDB-1	Feldspar		17.031	15.529	37.34	

TABLE 5 Sulfur Isotope (^{34}S) Characteristics of the Shuangdinggou and Xinling rock bodies.

Mining site	^{34}S (‰)	Data source
Shuangdinggou rock body	7.6	Dong et al. (2010), Duan et al. (2012)
	7.6	
	7.0	
Xinling rock body	6.3	
	6.3	
	5.6	

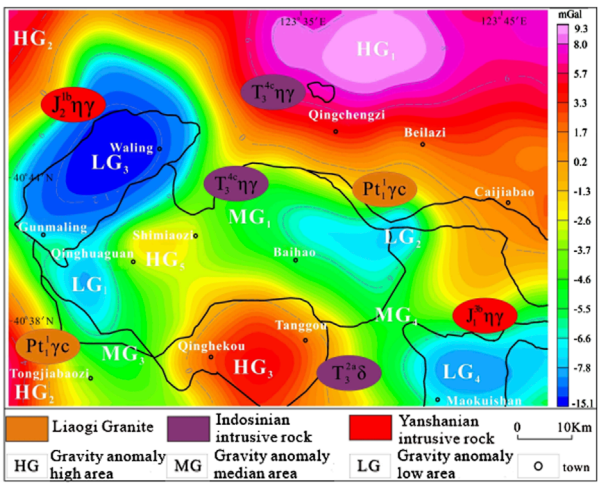

FIGURE 6
Plan view of the Bouguer gravity anomaly (1:50,000 regional Bouguer gravity of the Qingchengzi orefield).

power spectrum method effectively enhances residual gravity anomalies, both high and low, with clear morphological boundaries. These findings align well with the locations of exposed rock bodies at the surface. Moreover, the results from positional field separation serve as valuable data for inverse modeling, enhancing accuracy and reliability. Thus, this paper utilizes the radial power spectrum method for separating the residual anomalies.

The study utilized the radial mean power spectrum technique to assess local gravity anomalies and to partition gravity data into discrete segments. In the radial mean power spectrum of the Bouguer gravity anomaly depicted in Figure 8, the low-frequency regression line (①) denotes the mean depth of regional anomaly sources, while the high-frequency regression line (②) signifies the average depth of local anomaly sources within the gravity field.

Based on the power spectrum estimation of field source depth, the mean depth of regional and local anomalies can be calculated separately (Spector, 1970), as represented by Equation 1.

$$h = \frac{-(ln(P_2) - ln(P_1))}{2(r_2 - r_1)} \quad (1)$$

h: field source mean depth Unit: gravity anomaly sampling point interval.r: number of circular waves.ln (P): radial mean log power spectrum.

The average depth of the regional anomaly is determined by the coordinate intercept of the low-frequency regression line ①, as shown in Figure 9A.

$$r_2 = 0.4 \ln(P_2) = -10$$

$$r_1 = 0 \ln(p_1) = 6$$

$$h(\text{region}) = 20$$

The average depth of the local (residual) anomaly is obtained from the coordinate intercept of the low-frequency regression line ②, as shown in Figure 9B.

$$r_2 = 2 \ln(P_2) = -10$$

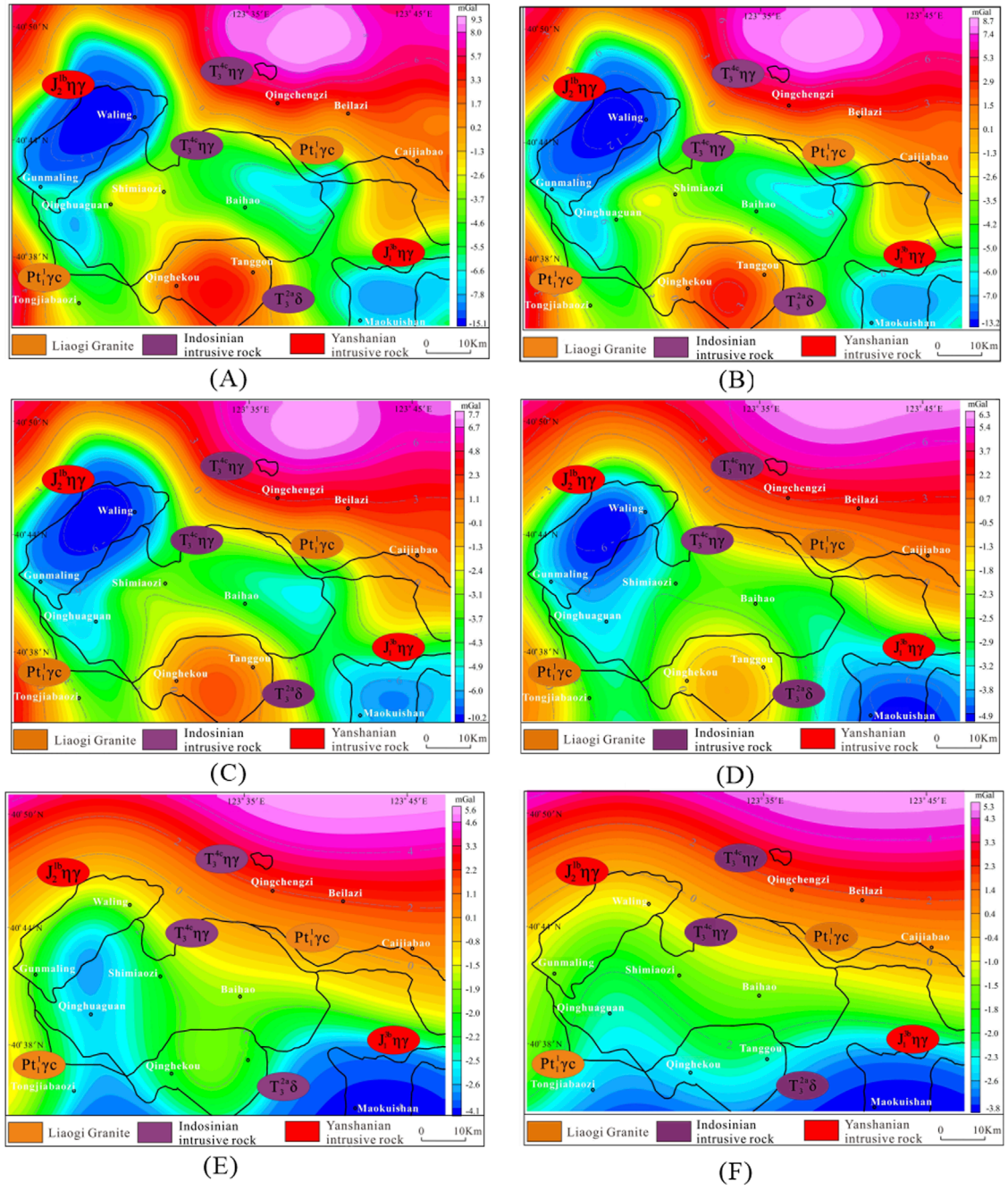

FIGURE 7
Plan view of the upward extension of the Bouguer gravity anomaly. **(A)** upward extension 500 m, **(B)** upward extension 1 km, **(C)** upward extension 2 km, **(D)** upward extension 5 km, **(E)** upward extension 8 km, **(F)** upward extension 10 km.

$$r_1 = 0.5 \ln(p_1) = -2$$

$$h(\text{local}) = 2.7$$

The unit of average depth (h) of the field source reflects the distance between gravity anomaly sampling points (see Figure 10). Based on the coordinates of these points throughout the area, the calculated distance measures 1989 m. To simplify the process, the gravity anomaly sampling points were established at intervals of 2,000 m.

The regional, localized average depth can be calculated as:

$$h(\text{regional}) \times 2\ \text{km} = 40\,\text{km}$$

$$h(\text{local}) \times 2\ \text{km} = 5.4\,\text{km}$$

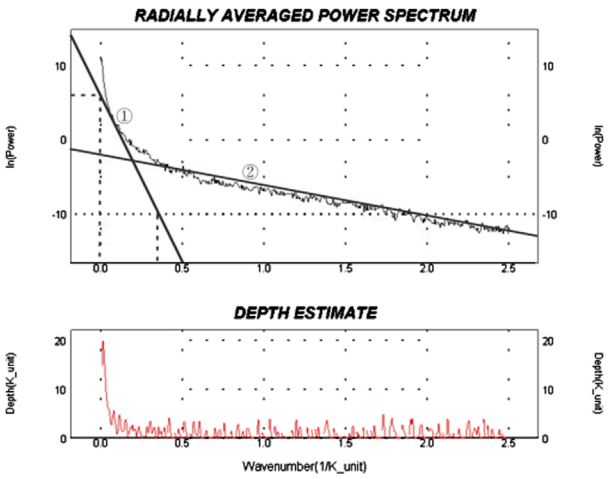

FIGURE 8
Radially averaged log power spectrum of the original gravity anomaly.

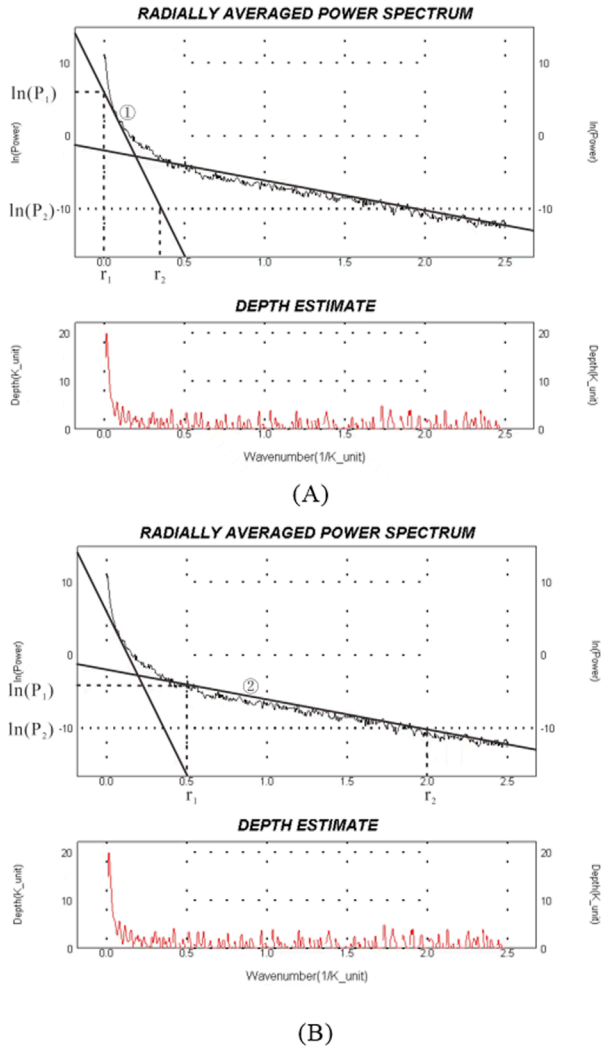

FIGURE 9
(A) Coordinate intercepts of the low-frequency regression line①; **(B)** Coordinate intercepts of the high-frequency regression line②.

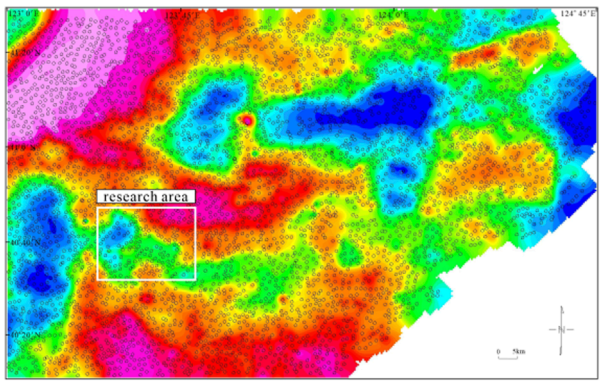

FIGURE 10
Gravity anomaly sampling sites in the study area.

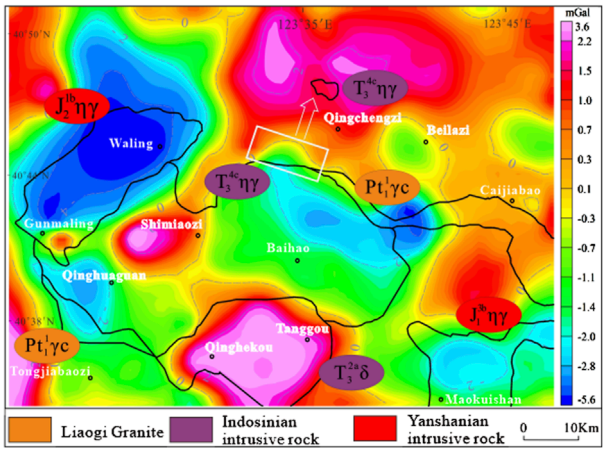

FIGURE 11
Residual gravity anomaly map (Using the Radially Averaged Power Spectrum method to obtain the residual gravity anomaly image).

The low-frequency regression line indicates an average depth of 40 km for the regional gravity anomaly. In contrast, the high-frequency regression line shows an average depth of 5.4 km for the local gravity anomaly. Analyzing the geological conditions in the area suggests that the average depth of the regional field source closely corresponds to the gravity anomaly created by the undulation at the base of the Anshan Group. This insight aids in understanding the underlying tectonic structure and the broader distribution characteristics of granite belts at depth. The local anomalous field source, located near the surface, primarily reveals the shallow geological structure and the local distribution of granite bodies. This source aligns with local gravity anomalies that stem from density differences between the shallow sedimentary cover and the intrusive rock body. A high-pass filter processed the original gravity field, which produced a local anomalous field (Figure 11).

Figure 11 illustrates that the local gravity anomaly fields, analyzed using the radial average power spectrum method, show varying enhancements in both high and low anomalies. The edges of these anomalies present distinct morphologies, correlating closely

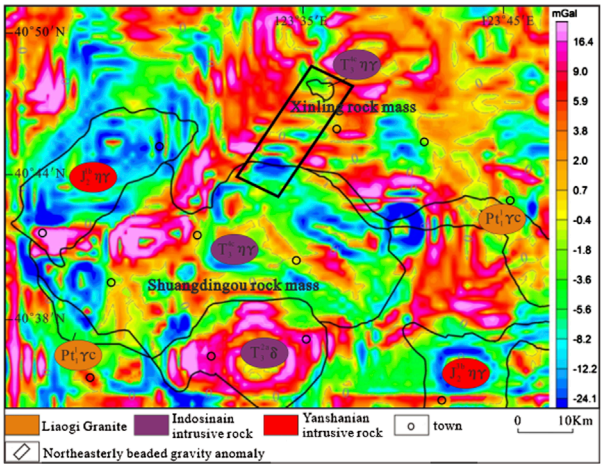

FIGURE 12
Plot of vertical second-order derivatives of local gravity anomalies.

with the positions of rock outcrops at the surface. The findings from their positional field separations can provide valuable data for inverse modeling, thereby improving accuracy and reliability. Furthermore, the median area of the local negative gravity anomaly located north of the Shuangdinggou rock body extends northeastward toward the Xinling rock body. This zone of negative gravity anomaly has surpassed the northern boundary of the Shuangdinggou rock body, reaching areas with high-density Liaohe Group strata. The negative gravity anomaly progressively transitions toward the Xinling rock body, aligning with the high-value zone of the positive gravity anomaly. Consequently, it can be inferred that a concealed extension exists northward from the Shuangdinggou rock body, directed toward the Xinling rock body. The median negative gravity anomaly results from the layering of high-density Liaohe Group strata above a low-density hidden rock body. This concealed section of the rock body, which is relatively shallow and limited in scale, gradually decreases toward the Xinling rock body, suggesting a northward-extending branch of the Shuangdinggou bedrock.

5.5 Vertical second-order derivative method

Certain anomalies might remain undetected in areas with complex or weak gravity anomaly signals. Yet, the vertical second-order derivative technique can alleviate gravitational influences resulting from deep regional geological factors. This method emphasizes geological anomalies nearer to the surface. Consequently, as illustrated in Figure 12, the localized gravity anomalies utilized their vertical second-order derivatives.

Figure 12 demonstrates that the regional deep gravity effect, which extends from the northern edge of the Shuangdinggou rock mass to the Xinling rock mass, experiences further suppression. This area shows a series of northeast-oriented clustered negative gravity anomalies where outcrops of high-density Liaohe Group strata are present. The lower values of these negative anomalies ($<-2.4 \times 10^{-5}$/mGAL) transition gradually to higher values (-0.18 to 0.1×10^{-5}/mGAL) (Figure 12). This trend indicates a gradual decrease in the burial depth of the rock body associated with the negative anomaly. It is posited that a concealed connection between the Shuangdinggou and Xinling rock masses extends significantly near the Shuangdinggou rock mass but diminishes towards the Xinling rock mass. Magma intrusion occurs within the Xinling rock mass along the Xinling Fault. Due to the limited extent of this concealed connection, local negative gravity anomalies become overshadowed by strong positive gravity anomalies from the overlaying Gao Liaohe Group strata, thereby masking any distinct low gravity anomaly presence.

5.6 Profile inversion

To thoroughly investigate the distribution pattern of the hidden connection between the Shuangdinggou and Xinling rock formations in the study area, researchers analyzed the local gravity anomaly data. Based on this methodology, they used the human-computer interaction profile inversion technique to offer a more quantitative assessment of the deep geological body's occurrence state.

The analysis focuses on the bead-like negative gravity anomalies aligned in the northeast between the Shuangdinggou and Xinling rock formations, as depicted in Figure 12. We selected cut profile AA', which intersects the center of each bead anomaly, and the validation profile BB', parallel to it on the western side of section AA' (Figure 1C). These profiles serve to validate the connectivity and distribution of the subsurface features within the two rock bodies. To ensure accuracy and credibility in the inversion calculations, we utilized MapGis, a Geographic Information System developed by the China University of Geosciences. This software allowed us to overlay the electronic geological map, local gravity anomalies, and elevation grid files (grid format) onto both profiles. This process extracted significant spatial data from the intersection of the profile line with geological boundaries, along with gravity anomalies and elevation values along the profiles. We then imported this profile inversion data into the GM-SYS module of OASIS Montaj Geophysical Data Interpretation Software from Geosoft. This software employs calibrated iterative inversion techniques, ranging from two-degree-half-body to three-degree-body approaches, along with real-time ortho-fitting methods. This methodology facilitates comparisons between the modeled gravity and magnetic responses and the measured anomalies, enhancing the interpretation of the data. Additionally, it supports the creation of an interactive underground geological model, which allows for validation of its accuracy. Figure 13 presents the gravity inversion results of the two anomalies.

In the study area, the foundation of the two inversion profiles consists of extensively distributed Liaoji granite, showing a density of 2.54 g/cm^3 along the profiles. The overall anticlinal structure of the Liaohe Group strata corresponds to the Xinling anticline. The Gaojiayu Formation at the base reaches a thickness of around 600 m and has a density of 2.72 g/cm^3. The Dashiqiao Formation ranges in thickness from 3,000 to 3,500 m, maintaining a density of 2.7 g/cm^3. The Gaixian Formation presents a thickness of 300 m and a density of 2.78 g/cm^3. The stratigraphic thickness declines toward the south and increases toward the north. The bottom boundary of the Shuangdinggou rock body lies at depths of 4,000–4,500 m. Notable connections exist between the Qingchengzi-Shuangdinggou and Xinling rock bodies, each exhibiting a density of 2.59 g/cm^3. Within

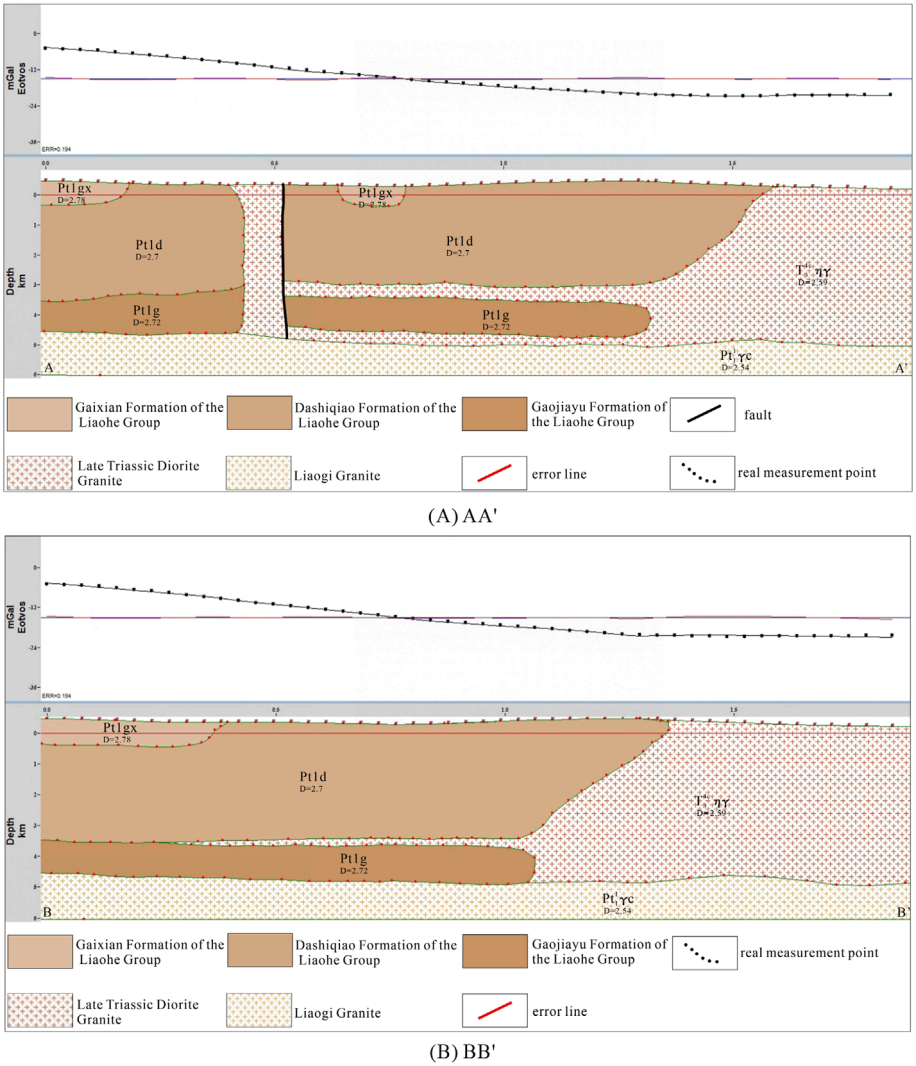

FIGURE 13
Local gravity anomaly map cut section inversion; **(A)** AA' gravity inversion profiles; **(B)** BB' gravity inversion profiles.

the two inversion profiles, magma from the Shuangdinggou base has penetrated the bases of both the Gaojiayu and Dashiqiao formations. This intrusion into the Gaojiayu and Dashiqiao formations occurs at a gentle angle, characterized by a minimal contact surface. The ore concentration area is concealed by the section connecting the Shuangdinggou and Xinling rock bodies. In the AA' profile, magma intrudes upwards, permeating the weak zone of the Xinling Fault within the Xinling anticline's core, resulting in the formation of the Xinling rock body. The Xinling rock body is marked by limited dimensions and shallow depth, while the Xinling Fault possesses a northeastern trend and an undercut depth of about 4,300 m. The BB' profile validates the findings of the AA' profile. The northern section of this profile does not intersect with the Xinling rock body, thus showcasing the intrusive relationship between the Liaohe Group stratigraphy and the Shuangdinggou rock body. The two inversion profiles align closely, with a discrepancy of 0.194 between actual and measured values, in close correlation with stratigraphic thickness, tectonic style, and fault positioning. Additionally, the rock density measurements of both profiles match the essential geological data of the region. The fitted line of the inversion gravity anomaly significantly aligns with its measured counterpart, indicating that the deep morphological distribution of the geological body illustrated by the profiles demonstrates accuracy and a high level of reliability.

6 Discussion

6.1 Metallogenic mechanisms and controlling factors of the Qingchengzi deposit

The amalgamation of geochemical and geophysical datasets has significantly enhanced our comprehension of the metallogenic processes and governing factors associated with the Qingchengzi Pb-Zn deposit. Geochemical investigations, encompassing the

distribution of rare earth elements (REE) and isotopic analyses, reveal that the Pb-Zn mineralization in this locale predominantly originates from magmatic-hydrothermal activities. The geochemical signatures imply that the ore-forming fluids were sourced from late Triassic magmatic intrusions, specifically the Shuangdinggou and Xinling granite bodies, which served as both the origin of these fluids and the repository for mineral deposition. A comparative analysis of the geochemical and geophysical findings indicates that the Pb-Zn mineralization is influenced not only by the composition and spatial distribution of the granite bodies but also by the structural characteristics of the region, including faults and fractures. These structural features likely functioned as conduits for the migration of hydrothermal fluids, which were crucial for the genesis of the Pb-Zn deposits. In summary, the metallogenic framework of the Qingchengzi deposit is attributed to magmatic-hydrothermal superposition, governed by both the regional tectonic context and deep-seated magmatic processes. The integration of geochemical and geophysical data offers a holistic perspective on the mineralization mechanism, emphasizing the critical role of subsurface structural features and fluid pathways in the formation of ore deposits.

6.2 Morphological extension of the concealed rock body

Through integrating geological data on stratigraphy, tectonics, and rock physical properties with statistical analyses of geochemical elemental characteristics from the Shuangdinggou-Xinling rock body, researchers established that the rock formation largely resulted from the melting of crustal materials. The ore-forming fluids mainly stemmed from magmatic-hydrothermal action, involving the interaction of magma and natural water. By interpreting Bouguer gravity anomaly data using upward extension techniques, a thorough analysis of the deep geological structure and the density variations among strata and intrusive rocks of varying ages and lithologies within the study area was achieved. Employing the radial average power spectrum method allowed for the field source separation of raw gravity data, determining local gravity anomalies and enhancing the accuracy of inversion modeling for field data. The human-computer interaction gravity profile inversion method disclosed the spatial relationship of the concealed connecting section of the Shuangdinggou-Xinling rock body at depth. Within the gravity inversion profile, the Shuangdinggou rock body appears as the main outcrop from the Indosinian period in the Qingchengzi ore area, with a burial depth of 4,000–4,500 m, facilitating substantial magma intrusion. Some magma intruded into the Gaojiayu Formation, reaching approximately 600 m deep, and into the bottom of the Dashiqiao Formation, extending to depths of 3,000–3,500 m, establishing intrusive contacts with the strata. Concurrently, it ascended along northeast-trending faults, promoting mineralization and transformation. Additionally, magma intruded into the tectonic weak zone at the juncture of the Xinling anticline core and the Xinling Fault, leading to the formation of the Xinling rock body, which manifested in a dendritic structure connected to the Shuangdinggou bedrock. By utilizing human-computer interaction profile inversion technology, a clear connectivity within the deeper sections of the Shuangdinggou-Xinling rock body became apparent. The hidden link between the Shuangdinggou and Xinling rock bodies in the ore concentration zone underpins the area's basement structure. This insight is crucial for analyzing geological structures and studying deposit genesis. The findings concerning the deep distribution of rock bodies indicate specific surface characteristics and complex hidden connections at depth, collectively forming an extensive magmatic system. This deep interconnection promotes the enrichment of Pb-Zn mineralization within the region.

6.3 Pb-Zn ore mineralization model in the Qingchengzi mining catchment area

During the Indosinian period, upwelling and downward intrusion caused magma to differentiate. Meanwhile, atmospheric precipitation percolated through faults into deep strata (Zhang et al., 2019a). The infiltrated water mixed with magma and fluids from magma differentiation to create high-temperature acidic hydrothermal fluids. This process involved continuous leaching, leading to the dissolution of ore-forming materials in the strata. The magma carried ore-bearing hydrothermal fluids that accumulated and precipitated in upward positions or favorable structural sections. This process ultimately formed layered ore bodies at the contact surface between the Gaojiayu Formation's base and the underlying hidden granite (Chen et al., 2024). At the fault intersection, ore-forming magmatic-hydrothermal fluids infiltrated the base of the Dashiqiao Formation, resulting in the precipitation of ore-forming elements and the creation of vein ore bodies. Feather-shaped Pb-Zn deposits formed near secondary fractures or rock veins close to the primary fault. Various combinations of magma intrusion events and contemporaneous faults, along with different early fold and fault combinations, influenced the formation and spatial distribution of ore bodies, serving as critical factors in ore control. Moreover, the Indonesian period's magmatic and tectonic activation led to the formation of the northeast-trending Erdaogou Fault, the northwest-trending Jianshanzi Fault, and secondary faults oriented nearly north-south and east-west within a diamond-shaped fault tectonic framework. These faults significantly affected the spatial distribution of Pb-Zn deposits, acting as transport pathways for metallogenic hydrothermal fluids necessary for the development of three distinct types of Pb-Zn deposits: layered, vein-like, and feathery. The scale and evolution of these ore-controlling faults directly influenced the migration of mineralizing elements, suggesting that regions with active magmatic or tectonic activity may present favorable conditions for exploring new deposits.

7 Conclusion

(1) The Shuangdinggou and Xingling rock formations exhibit a complex relationship, representing contemporaneous and homologous geologic structures. The Xinling formation intrudes into a weak structural zone at the intersection of the Xinling anticline core and the Xinling Fault, leading to a branching pattern that connects with the Shuangdinggou rock foundation. The Shuangdinggou formation boasts a significant

scale, with a burial depth ranging from approximately 4,000–4,500 m at its lower boundary. In contrast, the Xinling formation is relatively small in scale and demonstrates limited thickness.

(2) The hidden relationships between the Shuangdinggou and Xinling rock formations establish an intrusive interface with the overlying Paleoproterozoic sequences. Geochemical investigations, particularly focusing on the distribution of rare earth elements (REEs) and isotopic signatures, indicate that the mineralizing fluids were sourced from both geological bodies. Given the relatively shallow angle of intrusion, magmatic-hydrothermal fluids progressively permeated the Gaojiayu and Dashiqiao Formations. This sequence of events resulted in multiple hydrothermal layers, which ultimately facilitated mineralization during the Late Triassic, driven by hydrothermal superimposed transformation processes.

(3) Magma intrusion and fault activity play significant roles in shaping the development and distribution of Pb-Zn deposits. The Indosinian faults act as crucial conduits for the movement of ore-forming hydrothermal materials. Furthermore, the ancient Proterozoic strata located within the interaction zone between rock bodies and faults emerge as prime targets for predicting deep mineralization potential in the Qingchengzi ore concentration area.

Data availability statement

The original contributions presented in the study are included in the article/supplementary material, further inquiries can be directed to the corresponding author.

Author contributions

YL: Conceptualization, Data curation, Formal Analysis, Investigation, Methodology, Software, Validation, Visualization, Writing–original draft, Writing–review and editing. YY: Funding acquisition, Investigation, Methodology, Resources, Supervision, Validation, Writing–review and editing. XG: Formal Analysis, Investigation, Project administration, Resources, Writing–review and editing. HC: Investigation, Methodology, Resources, Writing–review and editing. JH: Investigation, Project administration, Resources, Writing–review and editing.

Funding

The author(s) declare that financial support was received for the research, authorship, and/or publication of this article. This research was funded by the National Natural Science Foundation of China (4150020180).

Acknowledgments

Thank you to the Editor-in-Chief of Editage for revising the paper and providing constructive review and suggestions. We thank the Editor-in-Chief and reviewers for their thoughtful reviews.

Conflict of interest

The authors declare that the research was conducted in the absence of any commercial or financial relationships that could be construed as a potential conflict of interest.

Generative AI statement

The author(s) declare that no Generative AI was used in the creation of this manuscript.

Publisher's note

All claims expressed in this article are solely those of the authors and do not necessarily represent those of their affiliated organizations, or those of the publisher, the editors and the reviewers. Any product that may be evaluated in this article, or claim that may be made by its manufacturer, is not guaranteed or endorsed by the publisher.

References

Al-Ghoul, M., and Sultan, R. (2019). Simulation of geochemical banding: theoretical modeling and fractal structure in acidization-diffusion-precipitation dynamics. *Phys. Rev. E* 100, 052214. doi:10.1103/PhysRevE.100.052214

An, Z. G., Di, Q. Y., Qu, W. Z., Zhang, Y., and Han, Y. (2022). Shallow crustal electrical structure of the Qingchengzi orefield in Liaodong area revealed by three-dimensional inversion of Magnetotelluric data. *J. Appl. Geophys* 202, 104650. doi:10.1016/j.jappgeo.2022.104650

Chen, J., Yang, F. C., Bedini, E., Chen, X. Y., Zhang, C. H., and Dong, H. (2024). Application of the matched filtering method to study the stream sediment geochemistry and prospecting prediction of the baiyun gold deposit, Qingchengzi ore field, China. *Min. Metall. Explor* 41, 379–394. doi:10.1007/s42461-023-00912-0

Chen, J. F., Yu, G., Xue, C. J., Qian, H., He, J. F., Xing, Z., et al. (2005). Pb isotope geochemistry of lead, zinc, gold and silver deposit clustered region, Liaodong rift zone, northeastern China. *Sci. China Ser. D-Earth Sci.* 48, 467–476. doi:10.1360/03yd0163

Chi, Y. K. (2002). Geochemical characteristics of ore-forming elements of the Qingchengzi ore field. *Geol. Resour.*, 109–118.

Di, Q. Y., Xue, G. Q., Zeng, Q. D., Wang, Z. X., An, Z. G., and Lei, D. (2020). Magnetotelluric exploration of deep-seated gold deposits in the Qingchengzi orefield, Eastern Liaoning (China), using a SEP system. *Ore Geol. Rev.* 122, 124. doi:10.1016/j.oregeorev.2020.103635

Dong, C. J., Zhang, H. T., and Zhan, B. C. (2010). Analysis of the metallogenesis of Qingchengzi Pb-Zn ore deposit. *Geol. Explor.* 46, 59–69.

Duan, X. X., Liu, J. M., Wang, Y. B., Zhou, L. L., Li, Y. G., Li, B., et al. (2012). Geochronology, geochemistry and geological significance of Late Triassic magmatism in Qingchengzi orefield, Liaoning. *Acta Petrol Sin.* 28, 595–606.

Duan, X. X., Zeng, Q. D., Wang, Y. B., Zhou, L. L., and Chen, B. (2017). Genesis of the Pb-Zn deposits of the Qingchengzi ore field, eastern Liaoning, China: constraints from carbonate LA-ICPMS trace element analysis and C-O-S-Pb isotopes. *Ore Geol. Rev.* 89, 752–771. doi:10.1016/j.oregeorev.2017.07.012

Duan, X. X., Zeng, Q. D., Yang, J. H., Liu, J. M., Wang, Y. B., and Zhou, L. L. (2014). Geochronology, geochemistry and Hf isotope of Late Triassic magmatic rocks of Qingchengzi district in Liaodong peninsula, Northeast China. *J. Asian Earth Sci.* 91, 107–124. doi:10.1016/j.jseaes.2014.05.009

Duan, X. X., Zhou, L. L., Zeng, Q. D., Wang, Y. B., Wang, Z. Q., and Yu, B. (2024). Superimposed multi-stage mineralization in the Qingchengzi Pb-Zn ore district, North China: evidence from geochronology and sulfide geochemistry. *Ore Geol. Rev.* 164, 105829. doi:10.1016/j.oregeorev.2023.105829

Ezzeddine, D., and Sultan, R. (2022). Bands, spherulites and 3D zonation in the carbonation of a slaked lime gel matrix. *J. Mol. Liq.* 346, 117089. doi:10.1016/j.molliq.2021.117089

Feng, Z. Q., Hao, W. B., Yuan, J., Liu, M., and Liu, Y. T. (2010). The savory taste enhancement in chicken soups. *Geol. Explor.* 46, 59–69.

Fu, L., Guo, J., Shen, W., Wang, X., Liu, X., Chen, X., et al. (2024). Geophysical evidence of the collisional suture zone in the prydz bay, east Antarctica. *Geophys. Res. Lett.* 51. doi:10.1029/2023gl106229

Gao, J. H., Li, W. M., Liu, Y. J., Zhao, Y. L., Liu, T. J., and Wen, Q. B. (2023). Detrital zircon LA-ICP-MS U-Pb ages of the North Liaohe Group from the lianshanguan area, NE China: implications for the tectonic evolution of the paleoproterozoic Jiao-Liao-Ji belt. *Minerals* 13, 708. doi:10.3390/min13050708

Hao, S., Houquan, Z., Jiangyu, W., Lei, S., Ming, L., Chuanxin, R., et al. (2023a). Prediction model for sandstone strength based on Weibull distribution of micro-element strength and power-law distribution of crack length. *J. Northwest. Polytech. Univ.* 41, 1114–1124. doi:10.1051/jnwpu/20234161114

Hao, S., Wenlong, C., Houquan, Z., and Lei, S. (2023b). A novel obtaining method and mesoscopic mechanism of pseudo-shear strength parameter evolution of sandstone. *Environ. Earth Sci.* 82, 60. doi:10.1007/s12665-023-10748-y

Hao, S., Wenlong, C., Houquan, Z., Song, L., Li, M., Wang, M., et al. (2023c). Dynamic strength characteristics of fractured rock mass. *Eng. Fract. Mech.* 292, 109678. doi:10.1016/j.engfracmech.2023.109678

He, J. C., Liu, J., Wang, X. T., and Hou, K. J. (2023). Genesis of Xinling Pb-Zn-Ag deposit in eastern Liaoning Province: evidences from zircon U-Pb age, sphalerite Rb-Sr age and H-O-S-Pb-He isotopic compositions. *Mineral. Deposits* 42, 331–346.

Ibrahim, H., Farah, H., Eddin, A. Z., Isber, S., and Sultan, R. (2017). Ag fractal structures in electroless metal deposition systems with and without magnetic field. *Chaos* 27, 083111. doi:10.1063/1.4997762

Ibrahim, Z., and Sultan, R. (2023). *In situ* infiltration-precipitation processes in some rock systems. *ACTA GEOCHIM.* 42, 870–878. doi:10.1007/s11631-023-00629-3

Jian, L., Changguo, D., Changwei, W., Mingchun, S., Changjiang, W., Shiyong, L., et al. (2023). Possible genetic relationship between Mesozoic magmatic rocks and gold mineralization in the Jiaodong Peninsula (Eastern China): constraints of magmatic evolution and physicochemical conditions. *Front. Earth Sci.* 11. doi:10.3389/feart.2023.1243844

Jianbiao, W., Runsheng, H., Yan, Z., Peng, W., Hongsheng, G., Lei, W., et al. (2024). Porosity-permeability characteristics and mineralization-alteration zones of the Maoping germanium-rich lead-zinc deposit in SW China. *Front. Earth Sci.* 12. doi:10.3389/feart.2024.1347243

Jiang, K. Y., and Liu, Z. H. (1990). Superposed Fold of Qingchengzi ore field liaoning province. *Contributions Geol. Mineral Resour.*, 22–35.

Jiang, S. Y., and Wei, J. Y. (1989). Geochemistry of the Qingchengzi LEAD-ZINC deposit. *Mineral. Deposits*, 20–28.

Li, D. D., Wang, Y. W., Qiu, J. Z., Wang, W., Li, S. H., Zhou, G. C., et al. (2020a). Chemical composition and prospecting significance of sulfides in Pb-Zn-Ag-Au deposits of the Qingchengzi ore concentration area, Liaoning Province. *Acta Petrologica Mineralogica* 39, 665–684.

Li, D. D., Wang, Y. W., Yang, Y. P., Qiu, J. Z., Xie, H. J., and Zhang, Z. C. (2023a). Indosinian magmatism and ore prospecting prediction in Qingchengzi area,Liaoning Province. *Mineral. Deposits* 42, 713–728.

Li, D. D., Wang, Y. W., Zhang, Z. C., Tian, Y., Zhou, G. C., Xie, H. J., et al. (2019a). Characteristics of metallotectonics and ore-forming structural plane baiyun gold deposit, Liaoning. *J. Geomechanics* 25, 10–20.

Li, J., Cai, W. Y., Li, B., Wang, K. Y., Liu, H. L., Konare, Y., et al. (2019b). Paleoproterozoic SEDEX-type stratiform mineralization overprinted by Mesozoic vein-type mineralization in the Qingchengzi Pb-Zn deposit, Northeastern China. *J. Asian Earth Sci.* 184, 104009. doi:10.1016/j.jseaes.2019.104009

Li, J., Cai, W. Y., Wang, K. Y., Kim, N., Liu, H. L., Lee, G. J., et al. (2020b). Initial decratonization of the eastern North China Craton: new constraints from geochronology, geochemistry, and Hf isotopic compositions of Mesozoic igneous rocks in the Qingchengzi district. *Geol. J.* 55, 3796–3820. doi:10.1002/gj.3635

Li, J., Dai, C. G., Wang, C. W., Song, M. C., Wang, C. J., Li, S. Y., et al. (2023b). Possible genetic relationship between Mesozoic magmatic rocks and gold mineralization in the Jiaodong Peninsula (Eastern China): constraints of magmatic evolution and physicochemical conditions. *Front. Earth Sci.* 11. doi:10.3389/feart.2023.1243844

Li, J., Wang, K. Y., Cai, W. Y., Sun, F. Y., Liu, H. L., Fu, L. J., et al. (2020c). Triassic gold-silver metallogenesis in Qingchengzi orefield, North China Craton: perspective from fluid inclusions, REE and H-O-S-Pb isotope systematics. *Ore Geol. Rev.* 121, 103567. doi:10.1016/j.oregeorev.2020.103567

Lin, W., Wang, Q. C., Wang, J., Wang, F., Chu, Y., and Chen, K. (2011). Late Mesozoic extensional tectonics of the Liaodong Peninsula massif: response of crust to continental lithosphere destruction of the North China Craton. *Sci. China-Earth Sci.* 54, 843–857. doi:10.1007/s11430-011-4190-5

Liu, J., Liu, F. X., Li, S. H., and Lai, C. K. (2019a). Formation of the Baiyun gold deposit, Liaodong gold province, NE China: constraints from zircon U-Pb age, fluid inclusion, and C-H-O-Pb-He isotopes. *Ore Geol. Rev.* 104, 686–706. doi:10.1016/j.oregeorev.2018.12.006

Liu, J., Zhang, L. J., Wang, S. L., Li, T. G., Yang, Y., Liu, F. X., et al. (2019b). Formation of the Wulong gold deposit, Liaodong gold Province, NE China: constraints from zircon U-Pb age, sericite Ar-Ar age, and H-O-S-He isotopes. *Ore Geol. Rev.* 109, 130–143. doi:10.1016/j.oregeorev.2019.04.013

Ma, Y. B., Bagas, L., Xing, S. W., Zhang, S. T., Wang, R. J., Li, N., et al. (2016). Genesis of the stratiform Zhenzigou Pb-Zn deposit in the North China Craton: Rb-Sr and C-O-S-Pb isotope constraints. *Ore Geol. Rev.* 79, 88–104. doi:10.1016/j.oregeorev.2016.05.009

Ma, Y. B., Du, X. H., Zhang, Z. J., Xing, S. W., Zou, Y. F., Li, B., et al. (2013). REE geochemical characteristics of Qingchengzi stratiform/veined Pb-Zn ore district. *Mineral. Deposits* 32, 1236–1248.

Ma, Y. B., Zhang, Y., Li, L. X., and Shen, H. F. (2022). Orogenic to post-orogenic transition of the Paleoproterozoic Jiao-Liao-Ji Belt: constraints from geochronology and geochemistry of the granites in the Qingchengzi area. *Acta Petrol Sin.* 38, 2971–2987. doi:10.18654/1000-0569/2022.10.05

Pengfei, W., Dapeng, L., Zhigang, S., Qiang, L., Ke, G., Yan, Z., et al. (2023). Petrogenesis and relationship with REE mineralization of the quartz syenite from Chishan and Longbaoshan alkaline complex, southeastern North China Craton: insights from zircon U-Pb geochronology, element, and Sr-Nd-Pb-Hf isotope geochemistry. *Front. Earth Sci.* 10. doi:10.3389/feart.2022.1046071

Quan, Y. K., Mu, M. S., Yang, D. B., Yan, X. Y., Wang, A. Q., Hao, L. R., et al. (2023). Geochronology and *in-situ* apatite geochemistry of late Paleoproterozoic A-type granites in the Jiao-Liao-Ji Belt, North China Craton: implications for petrogenesis and tectonic evolution. *Geochemistry* 83, 126009. doi:10.1016/j.chemer.2023.126009

Song, Y. H., Yang, F. C., Yan, G. L., Wei, M. H., and Shi, S. S. (2017). Characteristics of mineralization fluids and tracers of mineralization material sources of the Qingchengzi lead-zinc deposit in Liaoning Province. *Geol. Explor.* 53, 259–269.

Spector, G. (1970). To: statistical models for interpreting aeromagnetic data. *Geophysics*, 35, 293–302. doi:10.1190/1.1440092

Sun, G. T., Zeng, Q. D., Wang, Y. B., Li, B., and Chen, P. W. (2020a). Geochronology and geochemistry of Mesozoic dykes in the Qingchengzi ore field, Liaoning Province, China: magmatic evolution and implications for ore genesis. *Geol. J.* 55, 5745–5763. doi:10.1002/gj.3646

Sun, G. T., Zeng, Q. D., and Zhou, J. X. (2022). Machine learning coupled with mineral geochemistry reveals the origin of ore deposits. *Ore Geol. Rev.* 142, 104753. doi:10.1016/j.oregeorev.2022.104753

Sun, G. T., Zeng, Q. D., Zhou, L. L., Wang, Y. B., and Chen, P. W. (2020b). Trace element contents and *in situ* sulfur isotope analyses of pyrite in the Baiyun gold deposit, NE China: implication for the genesis of intrusion related gold deposits. *Ore Geol. Rev.* 118, 103330. doi:10.1016/j.oregeorev.2020.103330

Sun, X., Li, R., Si, X., Xiao, K., and Deng, J. (2024b). Timing and mechanism of ore precipitation in porphyry Cu systems: insight from LA-ICP-MS analysis of fluid inclusions and *in situ* oxygen isotope analysis of hydrothermal quartz at zhunuo porphyry Cu deposit, China. *Econ. Geol.* 119, 593–616. doi:10.5382/econgeo.5064

Sun, X., Li, R.-Y., Sun, H.-Y., Olin, P. H., Santosh, M., Fu, B., et al. (2024a). Genesis of Pb-Zn-Ag-Sb mineralization in the Tethys Himalaya, China: early magmatic-hydrothermal Pb-Zn(-Ag) mineralization overprinted by Sb-rich fluids. *Miner. Deposita* 59, 1275–1293. doi:10.1007/s00126-024-01264-5

Tan, W., Mao, Q. Q., Yu, M. J., Sun, Y., and Lv, X. Q. (2021). Mineralization of the tuwu porphyry Cu deposit in eastern tianshan, NW China: insights from *in situ* trace elements of chlorite and pyrite. *Front. Earth Sci.* 9. doi:10.3389/feart.2021.648177

Tannous, J., Anouti, L., and Sultan, R. (2018). Random spacing between metal tree electrodeposits in linear DLA arrays. *Entropy* 20, 643. doi:10.3390/e20090643

Wang, K. Y., Fu, L. J., Wei, L. M., and Wang, Z. G. (2016). Characteristics of hydrothermal superimposed mineralization and source of ore-forming fluids in Zhenzigou Pb-Zn deposit, liaoning province. *J. Jilin Univ. Sci. Ed.* 46, 80–90.

Wang, X. P., Peng, P., Wang, C., Yang, S. Y., Soderlund, U., and Su, X. D. (2017a). Nature of three episodes of Paleoproterozoic magmatism (2180 Ma, 2115 Ma and 1890 Ma) in the Liaoji belt, North China with implications for tectonic evolution. *Precambrian Res.* 298, 252–267. doi:10.1016/j.precamres.2017.06.003

Wang, Y. W., Xie, H. J., Li, D. D., Shi, Y., Liu, F. X., Sun, G. Q., et al. (2017b). Prospecting prediction of ore concentration area exemplified by Qingchengzi Pb-Zn-Au-Ag ore concentration area, eastern Liaoning Province. *Mineral. Deposits* 36, 1–24.

Wang, Y. Z., Wang, F., Shi, W. B., Yang, L. K., and Wu, L. (2020). Timing and processes of ore Formation in the Qingchengzi polymetallic orefield, northeast China: evidence

from 40Ar/39Ar geochronology. *Acta Geol. Sin-Engl Ed.* 94, 789–800. doi:10.1111/1755-6724.14370

Wei, L., Chuanxin, R., Hao, S., Shiqing, H., Bin, W., Yin, D., et al. (2022). Temporal and spatial evolution law of the freezing temperature field of water-rich sandy soil under groundwater seepage: a case study. *Processes* 10, 2307. doi:10.3390/pr10112307

Wei, P. F., Li, D. P., Song, Z. D., Liu, Q., Geng, K., Zhang, Y., et al. (2023). Petrogenesis and relationship with REE mineralization of the quartz syenite from Chishan and Longbaoshan alkaline complex, southeastern North China Craton: insights from zircon U-Pb geochronology, element, and Sr-Nd-Pb-Hf isotope geochemistry. *Front. Earth Sci.* 10. doi:10.3389/feart.2022.1046071

Wei, T., Qigui, M., Mingjie, Y., Yan, S., and Xiaoqiang, L. (2021). Mineralization of the tuwu porphyry Cu deposit in eastern tianshan, NW China: insights from *in situ* trace elements of chlorite and pyrite. *Front. Earth Sci.* 9. doi:10.3389/feart.2021.648177

Wu, J. B., Han, R. S., Zhang, Y., Wu, P., Gong, H. S., Wang, L., et al. (2024). Porosity-permeability characteristics and mineralization-alteration zones of the Maoping germanium-rich lead-zinc deposit in SW China. *Front. Earth Sci.* 12. doi:10.3389/feart.2024.1347243

Wu, J. J., Zhi, Q. Q., Deng, X. H., Wang, X. C., Chen, X. D., Zhao, Y., et al. (2022). Deep gold exploration with SQUID TEM in the Qingchengzi orefield, eastern liaoning, northeast China. *Minerals* 12, 102. doi:10.3390/min12010102

Xiao, C. H., Chen, Z. L., Yao, X. F., Liu, X. C., and Liu, J. M. (2023). The control of deformation partitioning on gold mineralization in the Qingchengzi district, Liaodong Peninsula, northeastern China. *J. Asian Earth Sci.* 242, 105517. doi:10.1016/j.jseaes.2022.105517

Xie, H. J., Wang, Y. W., Li, D. D., Shi, Y., Zhou, G. C., and Long, L. L. (2018). Geochronology and geochemistry study of the Shuangdinggou intrusion in the Qingchengzi ore concentration area, eastern liaoning province. *Acta Geol. Sin.* 92, 1264–1279.

Xie, H. J., Wang, Y. W., Li, D. D., Zhou, G. C., and Zhang, Z. C. (2021a). Late triassic magma mixing and fractional crystallization in the Qingchengzi orefield, eastern liaoning province: regional petrogenetic and metallogenic implications. *J. Earth Sci.* 32, 144–157. doi:10.1007/s12583-020-1114-3

Xie, T. T., Xu, T., Ai, Y. S., Zeng, Q. D., Zhang, W., and Zheng, F. (2021b). Imaging the shallow crustal velocity structure of the Qingchengzi ore field on the Liaodong Peninsula, China, with a short-period dense array using ambient noise tomography. *Tectonophysics* 813, 228913. doi:10.1016/j.tecto.2021.228913

Xu, L., Yang, J. H., Zeng, Q. D., Xie, L. W., Zhu, Y. S., Li, R., et al. (2020). Pyrite Rb-Sr, Sm-Nd and Fe isotopic constraints on the age and genesis of the Qingchengzi Pb-Zn deposits, northeastern China. *Ore Geol. Rev.* 117, 103324. doi:10.1016/j.oregeorev.2020.103324

Yang, J. H., Sun, J. F., Zhang, J. H., and Wilde, S. A. (2012). Petrogenesis of Late Triassic intrusive rocks in the northern Liaodong Peninsula related to decratonization of the North China Craton: zircon U-Pb age and Hf-O isotope evidence. *Lithos* 153, 108–128. doi:10.1016/j.lithos.2012.06.023

Yang, J. H., and Wu, F. Y. (2009). Triassic magmatism and its relation to decratonization in the eastern North China Craton. *Sci. China Ser. D-Earth Sci.* 52, 1319–1330. doi:10.1007/s11430-009-0137-5

Yang, Y. S., and Li, Y. Y. (2023). Ore-controlling structures of the Qingchengzi Pb-Zn-Au-Ag orefield, northeastern China and significance for deep ore prospecting: revealed from gravity and magnetic anomalies. *Ore Geol. Rev.* 156, 105376. doi:10.1016/j.oregeorev.2023.105376

Yang, Y. S., Pan, X. F., Hou, Z. Q., Deng, Y., Ouyang, Y. P., Meng, D. L., et al. (2021). Petrogenesis, redox state, and mineralization potential of triassic granitoids in the mengshan district, south China. *Front. Earth Sci.* 9, 09. doi:10.3389/feart.2021.657618

Yanshen, Y., Xiaofei, P., Zengqian, H., Yang, D., Yongpeng, O., Delei, M., et al. (2021). Petrogenesis, redox state, and mineralization potential of triassic granitoids in the mengshan district, south China. *Front. Earth Sci.* 9, 09. doi:10.3389/feart.2021.657618

Yu, G., Chen, J. F., Xue, C. J., Chen, Y. C., Chen, F. K., and Du, X. Y. (2009). Geochronological framework and Pb, Sr isotope geochemistry of the Qingchengzi Pb-Zn-Ag-Au orefield, Northeastern China. *Ore Geol. Rev.* 35, 367–382. doi:10.1016/j.oregeorev.2008.11.009

Yu, H., Zhao, G. C., Liu, J. M., Zhang, J. Q., Bi, G. Y., Guo, Q., et al. (2021). Analysis of structural characteristics of mineralization period in Qingchengzi Baiyun gold deposit in eastern Liaoning. *J. Jilin Univ. Sci. Ed.* 51, 1720–1739.

Yu, H. C., Liu, J., He, Z. H., Liu, Z. H., Cheng, C. Q., Hao, Y. J., et al. (2022). Geochronology and zircon Hf isotope of the paleoproterozoic Gaixian Formation in the southeastern Liaodong peninsula: implication for the tectonic evolution of the Jiao-Liao-Ji belt. *Minerals* 12, 792. doi:10.3390/min12070792

Zhang, P., Kou, L. L., Zhao, Y., Bi, Z. W., Sha, D. M., Li, Z. M., et al. (2019a). Fluid inclusions, H-O, S, Pb, and noble gas isotope studies of the Baiyun gold deposit in the Qingchengzi orefield, NE China. *J. Geochem Explor.* 200, 37–53. doi:10.1016/j.gexplo.2019.01.016

Zhang, P., Kou, L. L., Zhao, Y., Bi, Z. W., Sha, D. M., Li, Z. M., et al. (2019b). Fluid inclusions, H-O, S, Pb, and noble gas isotope studies of the Baiyun gold deposit in the Qingchengzi orefield, NE China. *J. Geochem Explor.* 200, 37–53. doi:10.1016/j.gexplo.2019.01.016

Zhang, Q. S. (1987). Early proterozoic crustal evolution of the east Liaoning peninsula. *Acta Geosci. Sin.*, 155–163.

Zhang, S. H., Zhang, Q. Q., Hu, G. H., Li, J. F., Xiao, C. H., Liu, X. C., et al. (2022a). Comparison of mineralization and preservation conditions in the Wulong and Qingchengzi ore concentration areas, eastern Liaoning Province: implications for deep metallogenic prediction. *Acta Geol. Sin.* 96, 232–248.

Zhang, Z. Q., Wang, G. W., Carranza, E. J. M., Yang, S. R., Zhao, K., Yang, W. D., et al. (2022b). Three-Dimensional pseudo-lithologic modeling via adaptive feature weighted k-means algorithm from multi-source geophysical datasets, Qingchengzi Pb-Zn-Ag-Au district, China. *Nat. Resour. Res.* 31, 2163–2179. doi:10.1007/s11053-021-09927-0

Zhou, G. C., Wang, Y. W., Li, D. D., Shi, Y., and Xie, H. J. (2017). LA-ICP-MS zircon U-Pb dating of dykes from the Baiyun gold deposit in eastern Liaoning. *Bull. Mineralogy, Petrology Geochem.* 36, 620–627.

Zhou, L. L., Zeng, Q. D., Liu, J. M., Duan, X. X., Sun, G. T., Wang, Y. B., et al. (2020). Tracing mineralization history from the compositional textures of sulfide association: a case study of the Zhenzigou stratiform Zn-Pb deposit, NE China. *Ore Geol. Rev.* 126, 103792. doi:10.1016/j.oregeorev.2020.103792